ABSTRACT

Title of Document: DEVELOPMENT OF ADVANCED WARPAGE MEASUREMENT SYSTEMS: SHADOW MOIRÉ WITH NONZERO TALBOT DISTANCE AND FAR INFRARED TWYMAN-GREEN INTERFEROMETRY

Austin Bradley Cox
Master of Science
2006

Directed By: Professor Bongtae Han
Department of Mechanical Engineering

Coefficient of thermal expansion mismatches in microelectronic devices induce deformation when these devices are subjected to thermal loading during manufacturing or everyday operation, creating failures and other reliability concerns. High-sensitivity out-of-plane deformation measurement systems are therefore required to characterize these deformations for design analysis and model verification. Two advanced systems improving on known techniques have been developed to fill needs not met by existing systems. A novel shadow moiré implementation using the nonzero Talbot distance overcomes fundamental limitations to conventional practice, providing an enhanced dynamic range uniquely capable of measuring large deformations and non-coplanar surfaces. In addition, an advanced interferometer using an infrared source enables characterization of rough surfaces

which are too diffusive for traditional visible interferometry. This system's Twyman-Green configuration also circumvents inherent limitations to previous Fizeau implementations. Results from experiments conducted on representative flip-chip specimens demonstrate both systems' unique capabilities.

DEVELOPMENT OF ADVANCED WARPAGE MEASUREMENT SYSTEMS: SHADOW MOIRÉ WITH NONZERO TALBOT DISTANCE AND FAR INFRARED TWYMAN-GREEN INTERFEROMETRY

By

Austin Bradley Cox

Thesis submitted to the Faculty of the Graduate School of the
University of Maryland, College Park, in partial fulfillment
of the requirements for the degree of
Master of Science
2006

Advisory Committee:
Professor Bongtae Han, Chair
Professor Avram Bar-Cohen
Professor Abhijit Dasgupta

ACKNOWLEDGEMENTS

I would like to take this opportunity to express my most sincere thanks to all of the people whose help and support made this work possible. Special thanks go out to my advisor, Dr. Han, for trusting me with this responsibility and contributing an endless supply of energy, advice, and generosity. I would also like to specifically acknowledge Kaushal Verma and Changwoon Han whose hard work laid the foundation for my project and made my job easy. I am additionally indebted to my friend and coworker John Dugan. His immense contributions to the design and implementation of the shadow moiré system make the system as much his as it is mine. Additional thanks go out to Yang for his custom analysis software, Dr. Post for his specimen holder design, and Steve and everyone else at Intel for their sponsorship and excessive kindness and generosity during my visit.

I would also be remiss if I did not acknowledge all of my mates in the lab over the years. Changwoon, Yuri, John, Seungmin, Hongbo, Samson, Ari, Chris, Nathan, and Yong, thanks for all of the help and great memories. It has been an honor working with such a wonderful group of friends. Special thanks also go to Ari for contributing suggestions and edits to this document.

Finally, I would like to thank my family. Mother, Father, and Travis, I am forever indebted for your love and support. I would also like to specifically acknowledge my father's editing contributions to this thesis.

TABLE OF CONTENTS

LIST OF FIGURES

CHAPTER 1: NEED FOR WARPAGE MEASUREMENT TECHNIQUES

1.1 Introduction

The mechanical design of microelectronic devices has garnered increased attention in recent years. Many issues which were ignorable at larger scales have become significant as these devices continue to push the limits in their size and complexity. A notable example is bending induced by coefficient of thermal expansion (CTE) mismatches within the device (Figure 1-1). Coupled with thermal cycling during the solder reflow process, such mismatches can induce uneven solder ball heights in the final assembly (Figure 1-2) [1]. This is an undesirable condition which can cause reliability issues for the entire product line and will only be exacerbated by new requirements for lead-free solder with its higher reflow temperature.

Bending can also be induced by heat generated within the device during normal operation. Repeated cycling as the device turns on and off can eventually lead to problems such as chip cracking, underfill delamination, and "pump out" of the conductive interstitial material used to transfer heat from the chip to the heat sink [1]. The device will usually fail should one of these conditions occur.

Realizing these correlations to device reliability, industry has developed an arsenal of high-sensitivity measurement techniques for characterizing deformations in microelectronic devices. These techniques provide experimental data which can be used to verify numerical modeling, making it possible to generate improved mechanical designs with higher reliability. Of the many available techniques, whole

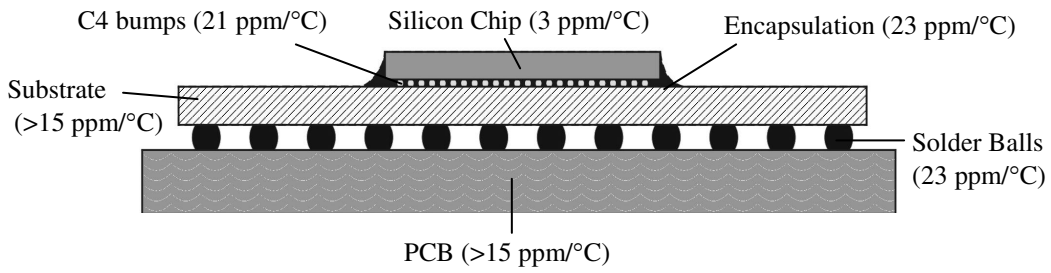

Figure 1-1: CTE mismatch in microelectronic devices (*modified from* [1])

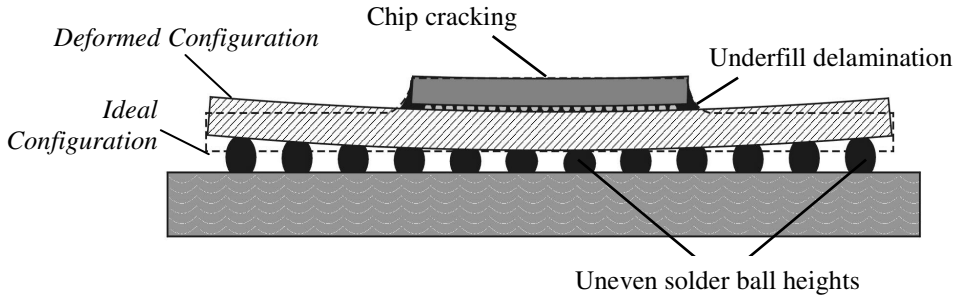

(a)

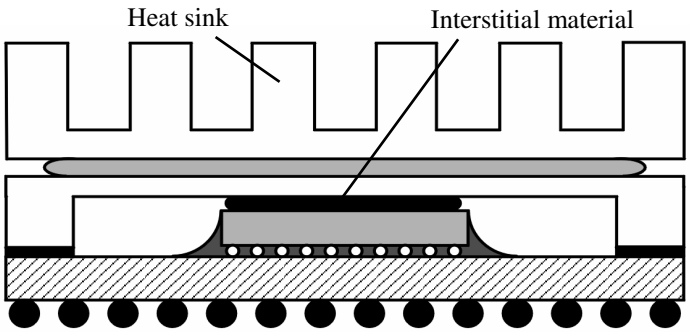

(b)

Figure 1-2: Common problems include (a) uneven solder ball heights induced during manufacturing, and chip cracking, underfill delamination, and (b) "pump out" of thermally conductive interstitial material between chip and heat sink after repeated cycling during operation (*modified from* [1]).

field techniques capable of characterizing every point on the specimen's surface simultaneously are generally best suited for taking measurements in a rapidly changing thermal environment; point measurement techniques are impractical due to this environment's inherently dynamic nature. All whole-field techniques fall into one of two classifications: out-of-plane techniques measure deformations normal to the viewing surface while in-plane techniques measure deformations in the plane of the viewing surface. A number of both types of techniques have been developed with a broad range of available sensitivities [2]. This affords the experimenter the ability to choose the technique best suited to the task at hand.

1.2 Phase Shifting Method

A number of measurement techniques display information in the form of fringe patterns: maps with contour lines connecting points of equal displacement. The contour interval is determined by the specifics of the employed measurement device. However, the overall sensitivity can be increased beyond this base value using an image processing technique known as phase shifting. In phase shifting, it is assumed that the intensity profile has a sinusoidal distribution as [3-5]

$$I(x, y) = a(x, y) + b(x, y)\cos[\phi(x.y) + \delta] \tag{1-1}$$

where a is the background intensity, b is the intensity amplitude of the fringe pattern, and Φ is the fringe pattern's phase at every point (x,y); conversely, δ is a constant phase shift for every point in the field. By closely controlling the specimen's motion, δ can be varied between 0 and 2π. Capturing at least three images for different values of δ makes it then possible to solve (1-1) for the three unknowns a, b, and Φ. The latter is of special importance as it provides information on what is happening

between the contours, extending the overall sensitivity beyond the measurement system's base capability. Assuming 8 bits-per-pixel digitization, the sensitivity can be enhanced a maximum of 256 times; however, 10 to 100 times improvement is generally accepted as a practically achievable range [5].

1.3 Objective of Work

The following chapters describe advanced implementations of two existing whole-field out-of-plane measurement techniques: shadow moiré and classical interferometry. Both systems were designed to resolve specific deficiencies in existing systems. In the case of the interferometer, a far infrared source enabled the testing of specimens with significant surface roughness that would be too diffusive for traditional visible interferometers. While similar work had been done previously [1], this system filled a stated need for an enlarged field of view and enhanced system stability. The shadow moiré system, on the other hand, realized a novel approach where the specimen is placed at the nonzero Talbot distance [4]. This increased the system's versatility and made it better suited for high-sensitivity measurements than the conventional implementation. Both systems were implemented in conjunction with an environmental oven to document co-planarity and warpage during thermal loading/cycling.

CHAPTER 2: FAR INFRARED TWYMAN-GREEN INTERFEROMETRY

2.1 Background and Motivation

2.1.1 Technical Review: Classical Interferometry

Classical interferometers operate on the principle of interference of coherent light. A laser creates a coherent beam, which is expanded and split into an *active beam*, which reflects off the specimen's surface, and a *reference beam*, which reflects off a known reference flat. These beams are then brought back together and focused onto an imaging plane. A fringe pattern results from interference between the flat reference wavefront and the active wavefront, which was distorted by the specimen's surface topography.

Two common optical configurations of classical interferometry are the Twyman-Green and Fizeau configurations (Figure 2-1). These designs differ in how they split the expanded laser beam. In the Twyman-Green configuration, a beam splitter physically separates the two beams, sending one to the specimen and the other to the reference flat. In the Fizeau configuration, an optical flat doubles as the beam splitter and reference flat, reflecting part of the beam toward the camera to serve as the reference beam and transmitting the rest through to the specimen. The latter serves as the active beam, reflecting off the specimen and passing back through the optical flat before entering the imaging system.

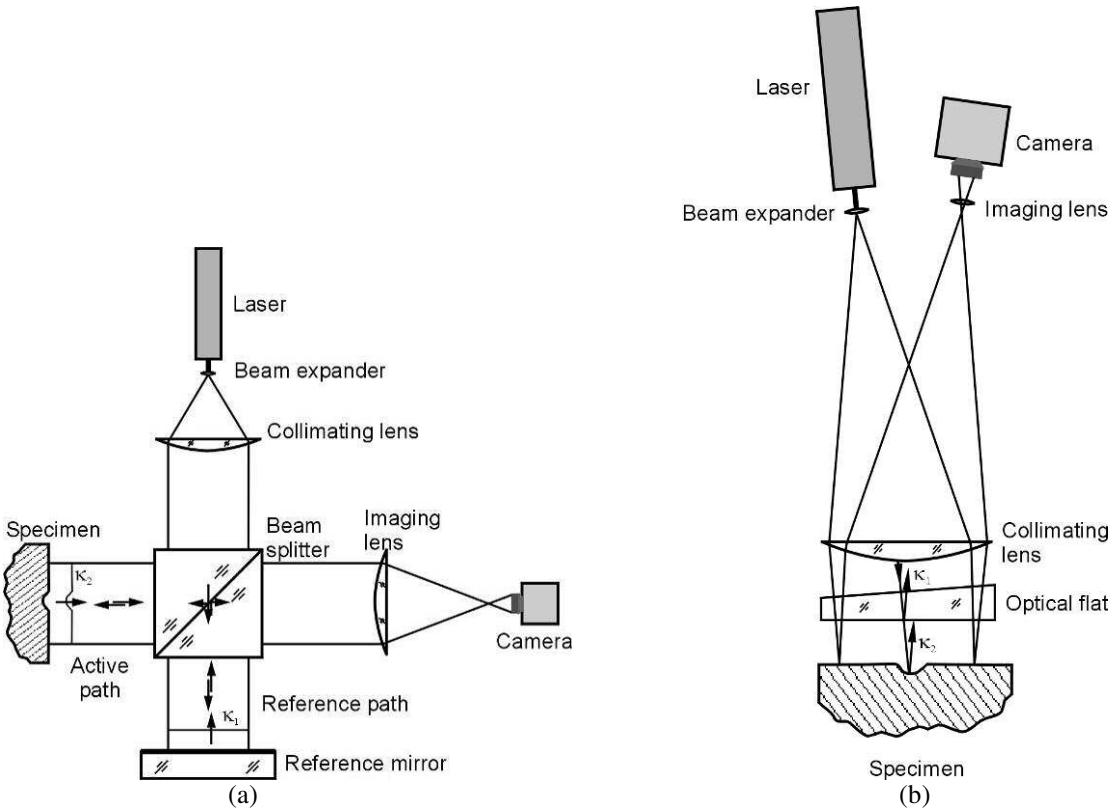

Figure 2-1: (a) Twyman-Green and (b) Fizeau configurations [2]

The governing equation for both interferometer configurations is given by [2]

$$W(x, y) = \frac{\lambda}{2} N(x, y) \tag{2-1}$$

where *W(x,y)* is the out-of-plane displacement, λ is the laser's wavelength, and *N(x,y)* is the fringe order. Both configurations have a contour interval equal to half the laser's wavelength ($\lambda/2$). Non-normal incidence is sometimes beneficial in the Fizeau configuration; in this case, the denominator of (2-1) becomes $2\cos\theta$, where θ is the angle of incidence on the specimen. However, θ is usually sufficiently small that the $\cos\theta$ term is neglected.

The minimal separation of the active and reference beams in the Fizeau configuration makes this design well suited for situations where fringe stability is a concern.

Because the two beams travel nearly identical paths, any environmental disturbances act on both beams equally, creating no relative wavefront distortions. Conversely, the significant separation of the active and reference beams in the Twyman-Green configuration makes this design more vulnerable to environmental disturbances acting on only one of the paths. As will be seen, however, the Twyman-Green design provides more flexibility in the positioning of its optical elements, an advantage that becomes more significant with the introduction of an environmental oven.

2.1.2 Technical Review: Rayleigh Criteria for Rough Surfaces

Interferometers inherently require a mirror-like (*specular*) specimen surface. Instead of providing the camera with a concentrated reflection, a non-specular (*diffusive*) surface will disperse the active beam. In many cases, surface roughness is to blame for a surface's diffusivity; microscopic surface imperfections randomly reflect radiation in all directions regardless of the angle of incidence to the mean surface (Figure 2-2). Surface preparation techniques such as polishing and metal deposition can make such surfaces artificially specular; however, these methods are time consuming to perform and may alter the specimen's natural deformation.

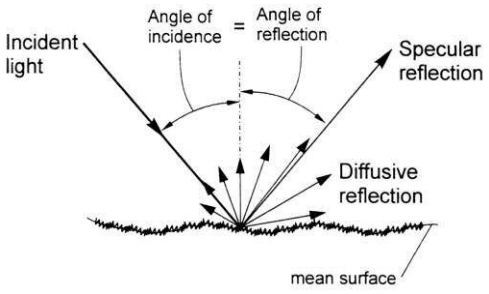

Figure 2-2: Incident radiation diffused by excessive surface roughness [1]

Inspired by Beckmann and Spizzichino's studies into the scattering of electromagnetic waves by randomly rough surfaces [6], far infrared interferometry reduces the diffusive effects of surface roughness by increasing the wavelength of the light in relation to the height of surface irregularities *h*. This has been described quantitatively by the Rayleigh criterion [6,7]

$$\varepsilon_r = \frac{4\pi h \cos\theta}{\lambda} \tag{2-2}$$

where ε_r is an *effective roughness factor*. Per (2-2), the effective roughness is inversely proportional to the incident wavelength, implying that surfaces that were diffusive under visible illumination will appear specular under illumination by a significantly longer wavelength. This concept inspired the development of the first infrared interferometer by Munnerlyn and Latta [8]. This and later systems employed a CO_2 laser with a wavelength of 10.6 μm, thereby reducing the effective surface roughness by a factor of nearly 20 compared with that seen under visible illumination [1,7-11].

2.1.3 Prior Work: Far Infrared Fizeau Interferometry

The surface roughness of many microelectronic components and materials such as silicon served as the motivation behind Verma and Han's Far Infrared Fizeau Interferometer (FIFI) [1,9,10]. A CO_2 laser and specialized Zinc Selenide (ZnSe) optics were employed to achieve a Fizeau interferometer at λ = 10.6 μm. A

convection oven was incorporated to test components during thermal cycling. The system's field of view ranged from 0.5" by 0.5" to 1.75" by 1.75".

The Fizeau design was chosen to minimize the difficulty of tuning the invisible infrared beam. Its minimal physical separation of the active and reference beams also improved system stability by mitigating the impact of air's variable refractive index inside the environmental oven. Additionally, the design's reuse of the collimating lens as the imaging field lens minimized optical aberrations; any distortions induced when the beam passed forward through the lens were partially offset when the beam passed back through in the opposite direction [1].

2.1.4 Motivation: Need for Far Infrared Twyman Green Interferometry

The Fizeau configuration used in FIFI required that the optical flat be held inside the oven with the specimen. To avoid oven vibrations, the flat was connected directly to the optical table via rods passing through holes in the oven wall. The need for phase shifting for sensitivity enhancement further required that a stepper motor be incorporated into this stage. The result was a bulky design that was poorly suited for providing accurate and reliable phase shifting and satisfactory fringe stability, a problem that would only be exacerbated if a larger optical flat were used to increase the system's field of view.

The physical separation of the active and reference paths in the Twyman-Green design makes this configuration well-suited for overcoming the inherent limitations to

the Fizeau design. More specifically, while Fizeau requires the reference flat to be located inside the environmental oven with the specimen, Twyman-Green's path separation allows the flexibility to position all of the optical components, including the reference flat, outside the oven (Figure 2-3). This makes the reference flat more readily accessible to the user for making fringe pattern adjustments and, more importantly, eliminates the inherent difficulty in FIFI of holding this element inside the oven in a manner that is both stable and conducive to phase shifting. The Far Infrared Twyman-Green Interferometer (FITGI) is therefore proposed to meet industry's need for an out-of-plane measurement system that retains the benefits of far infrared interferometry while improving on difficulties encountered with the Fizeau design and accommodating increasingly large fields of view.

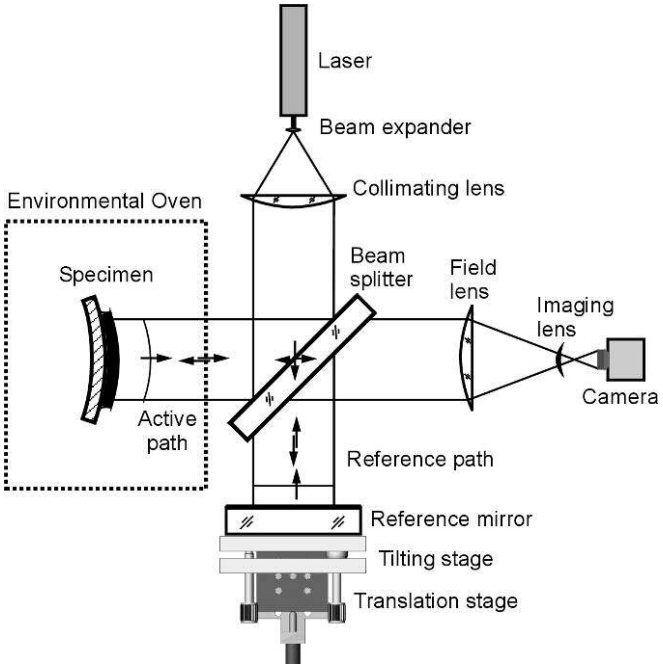

Figure 2-3: Simplified FITGI optical configuration showing the external mirror and translation stage.

2.1.5 Prior Work: Far Infrared Twyman-Green Interferometry

Several previous far infrared Twyman-Green interferometers have taken advantage of the benefits offered by infrared's longer wavelength. Kwon, et al.'s system was used to test the surface of specialized optics [11] while that of Sinha and Tippur was used in a wide range of applications including defect detection and crack tip-field mapping [7]. These interferometers had effective beam diameters of only 20 mm and 35 mm, respectively, resulting in limited fields of view. Further, neither system incorporated an environmental oven, making them ineffective for simulating thermal loading in microelectronic devices. While similar in design to these previous interferometers, the FITGI system uniquely incorporates an environmental oven for thermal loading. In addition, an approximately 70 mm effective beam diameter provides an expanded field of view. These benefits came at the cost of several notable design challenges, to be discussed later.

2.2 Design Requirements

To effectively characterize the larger devices being developed by the microelectronics industry, the FITGI had to accommodate fields of view up to 2" by 2". In addition to eliminating the impractical optical flat stage of FIFI, the FITGI was also required to improve on the conventional specimen holder design where the specimen is mounted on a vertical stage using double-sided tape (Figure 2-4) [1]. The specimen's vertical orientation made the FIFI system unsuitable for certain applications, such as characterizing deformation during epoxy underfill curing, solder reflow, etc. The mounting tape also unnaturally constrained the specimen's deformation. To

overcome these issues, the FITGI system implemented a simple horizontal plate specimen holder (Figure 2-4). This design introduces no external constraints on the specimen's deformation and makes the FITGI more versatile than its predecessor.

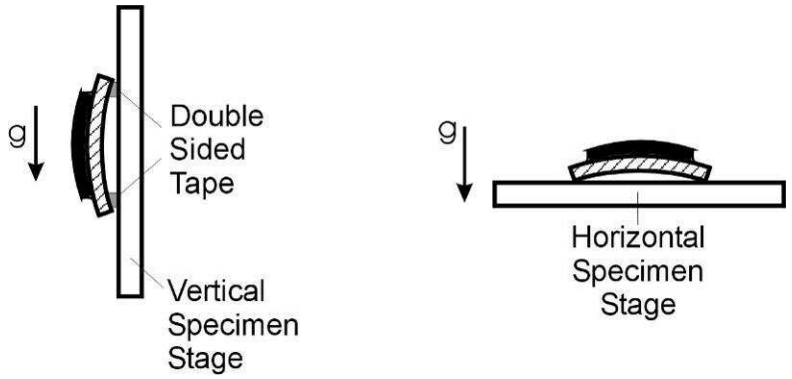

Figure 2-4: (a) Vertical and (b) horizontal specimen stages used in FIFI and FITGI, respectively

2.3 Final Design Overview

2.3.1 Mechanical Configuration

Being an interferometer, the FITGI system required a coherent laser light source for illumination and a camera for imaging. Other required hardware included an environmental oven for thermal cycling and a translation system for phase shifting. These components were connected through a personal computer (Figure 2-5) in which a custom LabView application coordinated operation of the individual devices per the user's instructions. This control software will be discussed in greater detail in Chapter 4.

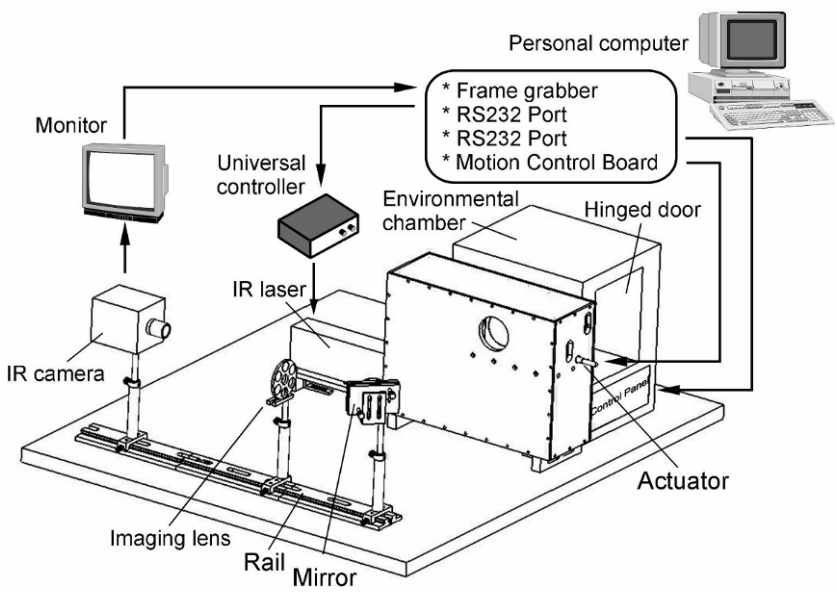

Figure 2-5: FITGI mechanical configuration

As with previous far infrared interferometers [1,7-11], a CO_2 laser was chosen as the light source to take advantage of its long 10.6 μm wavelength. Because CO_2 lasers are typically used for high power applications such as metal cutting and engraving, the 10-watt, model 48-1 from Synrad was the lowest power option on the market. During operation, the laser's power was typically kept between one- and three-watts by a Synrad UC-1000 universal controller. This range avoided both the intensity instabilities observed at extremely low power and the need for air cooling at higher power levels. The beam produced by the 48-1 was vertically polarized and had a diameter of 3.5 mm.

A Synrad laser diode pointer was mounted to the faceplate of the CO_2 laser and was an essential tool for aligning and tuning the optical system. The pointer emitted a

visible red beam that, when co aligned with the CO_2 beam, made it possible to track the path of the invisible infrared beam through the interferometer.

An Electrophysics PV320 infrared camera was used for imaging. This camera used a 320 by 240 array of pyroelectric elements, which respond to changes in temperature. To image under constant intensity, the camera implemented a chopper to alternately block and pass the infrared beam, allowing the detector elements time to cool and heat, respectively. The camera was connected to a Pulnix SV5 frame grabber on the control computer via a BNC cable. The LabView control program displayed the video to the screen and enabled image capture.

A model EC1A oven from Sun Electronic Systems served as the system's convection chamber. This unit used an integrated electric heater and an external liquid nitrogen tank for heating and cooling, respectively, and was rated for a maximum ramp rate of 30 ºC/min. A custom 3.5" diameter port in the side wall held a double-paned window for viewing the specimen. In addition, a smaller 2" diameter port in the same wall provided a through-hole for securing the specimen holder from outside the oven. Communication between the oven and the control computer occurred through a serial connection.

Phase shifting was accomplished using a Thorlabs MT1-Z6 translation stage driven by a Thorlabs Z612B half-inch motorized actuator. The actuator's 0.5 mm pitch lead screw and 12,288 counts-per-revolution optical encoder enabled submicron

positioning control (40.7 nm per step), making the translation system well suited for phase shifting within the interferometer's 5.3 μm contour interval. A Thorlabs DCX-PCI100 motion control card managed the actuator's motion as instructed by the control software. The reference flat was connected to the translation assembly through a tilting stage, providing a means of tuning the system and adjusting the fringe pattern.

2.3.2 Optical Configuration

Glass's poor transmissivity in the far infrared spectrum made it necessary to consider more exotic materials for the system's optical elements. Zinc Selenide (ZnSe) was chosen for this need because the transmission range of ZnSe covers both the infrared and visible spectrums; therefore, ZnSe optics transmit both the infrared beam and the red alignment beam [1,9-11]. Alternative infrared optical materials such as Germanium were impractical due to their poor transmissivity of visible light.

The optical configuration of FITGI (Figure 2-6) was divided into two largely independent subsystems: a beam expansion system for illuminating the specimen and reference flat, and an imaging system for focusing the active and reference beams on the camera sensor. Once tuned, the beam expansion system should remain fixed. Conversely, the imaging system must allow adjustability to accommodate several fields of view.

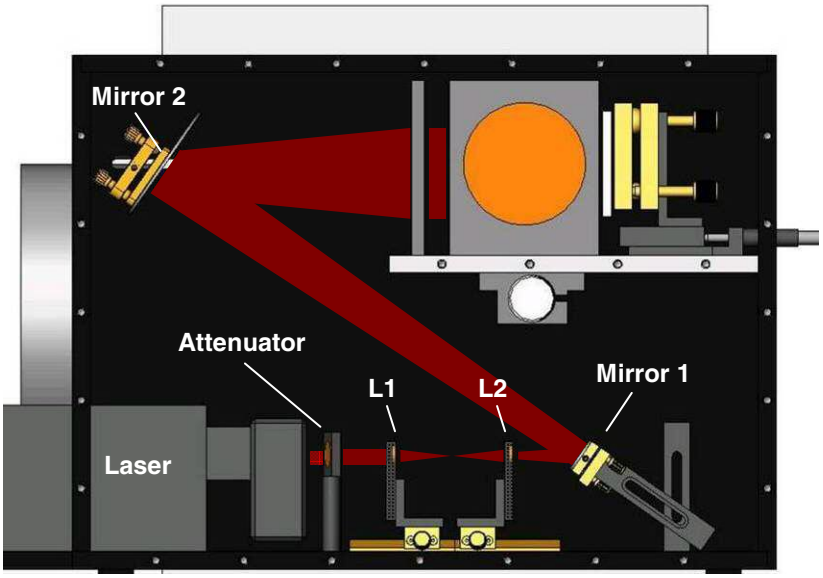

(a)

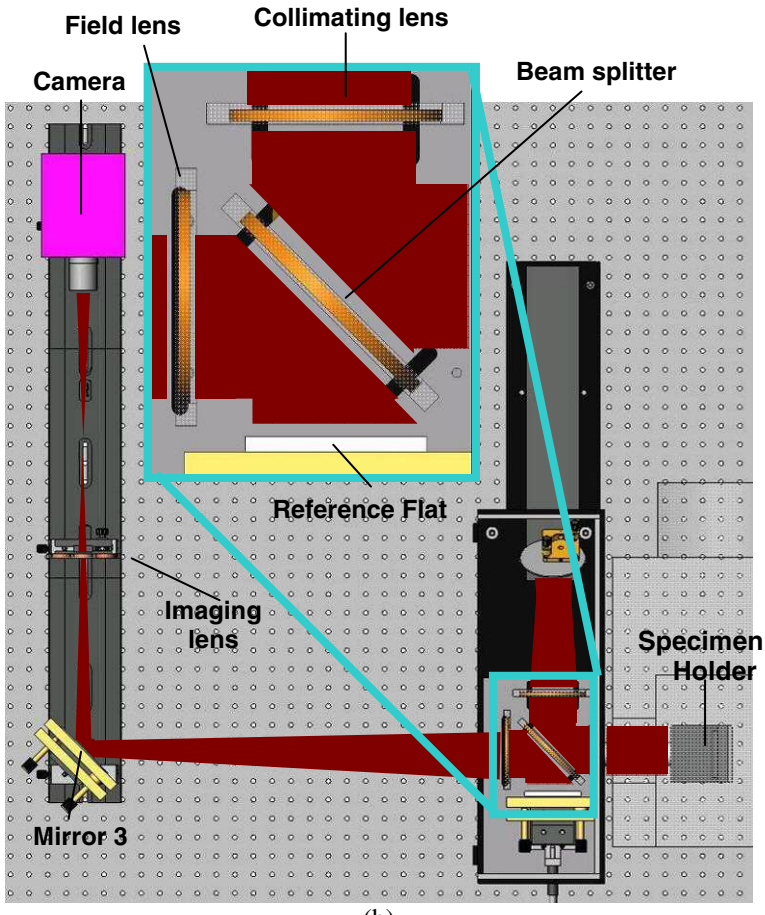

(b)

Figure 2-6: Optical configuration (a) Side and (b) Top Views (L1: Planoconvex lens, L2: Planoconcave lens)

The beam expansion system began with an attenuator, which reduced the laser beam's intensity to a serviceable 10% of its output level. A pair of small planoconvex (focal length f = 1") and planoconcave (f = -2") lenses diverged the beam, which expanded as it traveled through a "Z"-shaped path to a 3.5" diameter collimating lens (f = 25"). The "Z" shaped expansion system, which was achieved using two silicon mirrors, made the system more compact than if expansion occurred over a direct line. After collimation, a beam splitter separated the beam into the active and reference paths.

After reflection off the specimen and reference flat, the active and reference paths recombined at the beam splitter. The beams then passed into the imaging system where a 3.5" diameter field lens (f = 40") collected the large diameter beams and converged them toward a third silicon mirror. Reflections off this mirror passed through a 1" diameter meniscus imaging lens and into the camera. Again, the mirror was used to make the system more compact by reducing the required footprint.

A lens wheel provided a selection of four meniscus imaging lenses with varying focal lengths for adjusting the system's field of view. The system could accommodate fields of view between 0.5" and 2.0" depending on the selection of the imaging lens and the relative locations of the field lens, the imaging lens, and the camera (Table 2-1). The camera and imaging lens wheel were located on an optical rail to facilitate positioning adjustments.

Imaging Lens Focal Length (in.)	Field Lens to Imaging Lens Distance (in.)	Imaging Lens to Camera Distance (in.)	Resultant Field of View (in.)
15.0	23.4	25.3	0.5
12.0	33.6	16.1	1.0
9.0	35.0	11.1	1.5
7.5	37.8	8.8	2.0

Table 2-1: FITGI imaging system configurations for select fields of view

Two 3.5" ZnSe windows were installed into the large oven port, providing a means of the viewing the specimen during thermal cycling. The double-paned design provided increased insulation and, more importantly, minimized frost condensation at subzero temperatures. The windows were coated with an antireflection (AR) coating on both sides to avoid introducing additional beams into the imaging system. As the coatings were not perfectly effective, the oven was slightly angled with respect to the active and reference beams to direct any reflections off the windows away from the imaging system.

The optical flat used in the FIFI design had to transmit light through to the specimen; therefore, it was made from ZnSe like the rest of the optical components. The separation of the active and reference paths in the Twyman-Green design, on the other hand, allowed more flexibility in choosing the reference flat's material. The key consideration for the FITGI was the contrast of the captured fringe pattern, which is a function of the intensity of the active and reference beams per the equation [2]

$$\%\,\text{contrast} = \frac{I_{\max} - I_{\min}}{I_{\max}} \times 100\% \tag{2-3}$$

where I_{max} and I_{min} are given by the equation for impure two-beam interference [2]

$$I = I_1 + I_2 + 2\sqrt{I_1 I_2}\cos 2\pi \frac{S}{\lambda} \tag{2-4}$$

$$\Rightarrow I_{\max} = I_{active} + I_{ref} + 2\sqrt{I_{active} I_{ref}}$$
$$I_{\min} = I_{active} + I_{ref} - 2\sqrt{I_{active} I_{ref}}$$

As the interferometer had to accommodate materials with varying reflectivities, fringe contrast was plotted as a function of the reference flat reflectivity for a wide range of specimen reflectivities (Figure 2-7). With a reflectivity of 4%, glass exhibited exceptional contrast for specimen reflectivities between 1% and 30%. Acceptable contrast (≈ 50%) was also obtained for metallic coatings with reflectivities up to 100% and low reflectivity materials down to around 0.1%. This broad range made a glass optical flat a practical choice for the system's reference flat.

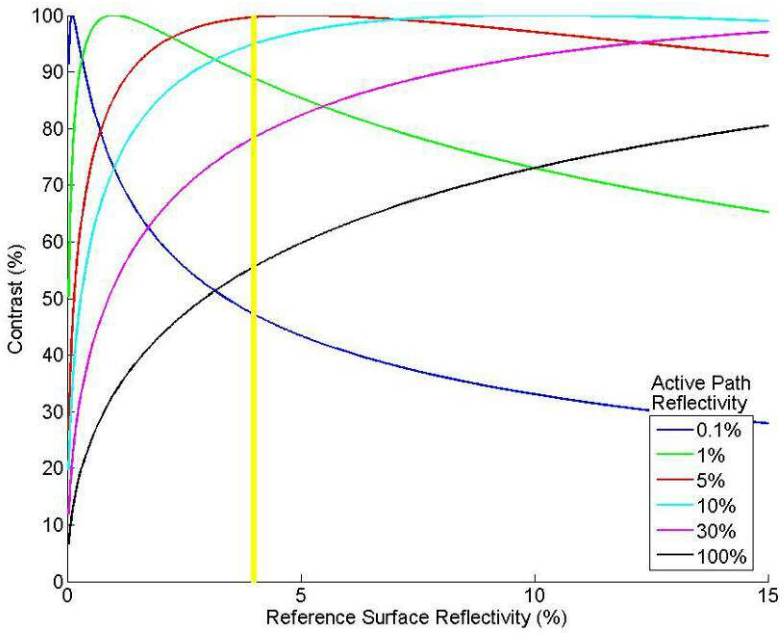

Figure 2-7: Fringe pattern contrast as a function of reference surface reflectivity for selected active path reflectivities. The yellow line indicates the reflectivity of glass (4%)

2.4 Technical Challenges

2.4.1 Beam Splitter Design

The most significant technical challenge encountered while moving from Fizeau to Twyman-Green was the design of the beam splitter, which was not used in the former configuration but is crucial to the latter. As was the case with all of the system's optical elements, the beam splitter was made of ZnSe because of this material's excellent optical properties in both the visible and far infrared spectrums.

As shown in Figure 2-8, a beam splitter with a reflectivity of 50% makes the most efficient usage of available intensity. In this case, 50% of the total incident light makes it into the imaging system, with the active and reference paths contributing an equal 25% share. The remaining 50% of the incident light is reflected back in the direction of the source. Deviation from 50% beam splitter reflectivity in either direction results in a decrease in the intensity seen by the imaging system, with a minimum of 0% intensity seen by the imaging system when the beam splitter has a reflectivity of either 0% or 100%.

Glass windows used as beam splitters in traditional visible light interferometers typically require thin-film coatings to increase their reflectivity. This necessity owes to the low reflectivity of bare glass caused by glass's relatively low index of refraction ($n \approx 1.5$ at $\lambda = 633$ nm). Per Fresnel's equations for dielectric media, the intensity reflection coefficient is given by [12]

$$R_{\perp} = \left(\frac{\sin(\theta_i - \theta_t)}{\sin(\theta_i + \theta_t)} \right)^2 \tag{2-5}$$

for polarization perpendicular to the plane of incidence and [12]

$$R_{\square} = \left(\frac{\tan(\theta_i - \theta_t)}{\tan(\theta_i + \theta_t)} \right)^2 \tag{2-6}$$

for polarization parallel to the plane of incidence. Here, θ_i is the angle of incidence and θ_t is the angle of transmission given by the well-known Snell's law

$$n_i \sin\theta_i = n_t \sin\theta_t \tag{2-7}$$

The maximum reflectivity of glass at 45° incidence is therefore $R_{\perp} \approx 9\%$, resulting in only 17% of the incident light reaching the imaging system per Figure 2-8. This is an unacceptable amount of intensity loss in most cases.

Conversely, the maximum reflectivity of ZnSe at 45º incidence is $R_{\perp} \approx 28\%$ thanks to the high index of refraction of ZnSe ($n \approx 2.4$ at λ = 10.6 μm). Per Figure 2-8, this results in approximately 40% of the incident intensity reaching the imaging system, which is sufficient for most purposes. Therefore, while glass windows used as beam splitters in traditional visible light interferometers require a reflectivity-enhancement coating, a bare ZnSe window surface should suffice for use as a beam splitter in far infrared interferometry.

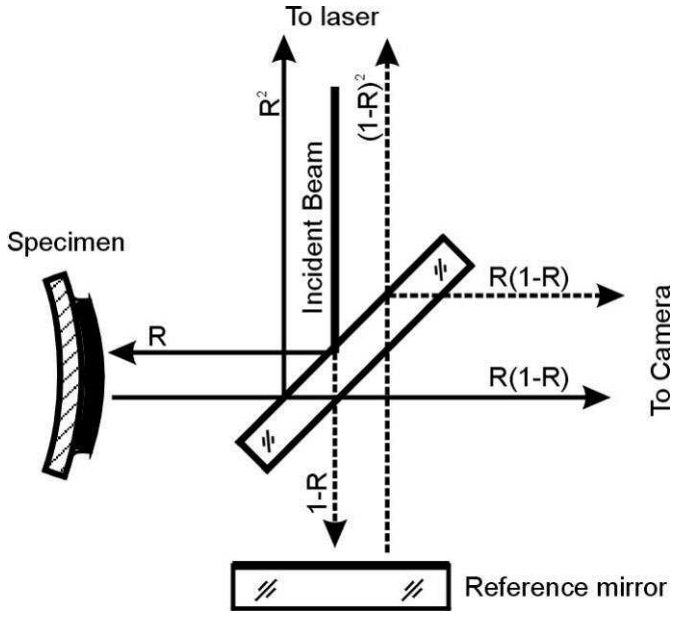

(a)

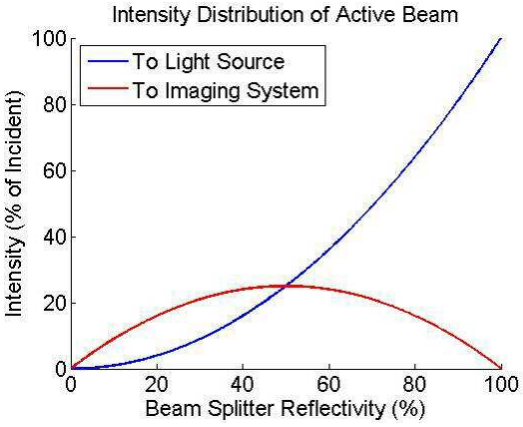

(b)

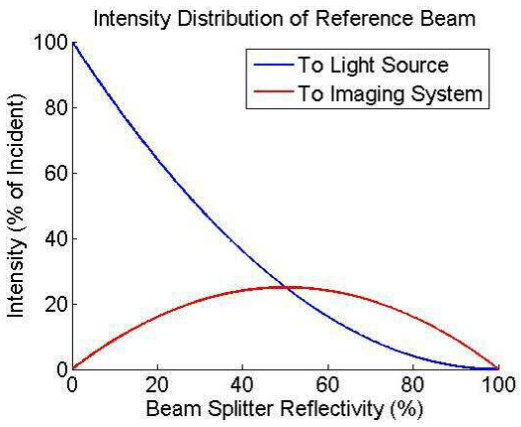

(c)

Figure 2-8(a): Intensity distribution around the beam splitter (R = beam splitter reflectivity); and intensity distribution as a function of beam splitter reflectivity for the (b) Active and (c) Reference paths

The previous analysis ignored reflections from the window's second surface which complicate the situation through the introduction of an additional set of active and reference beams. Visible interferometers traditionally handle these beams, which can distort the desired "true" fringe pattern, by applying an antireflection (AR) coating to the second surface. While this solution does not prevent the undesired beams from entering the imaging system, an effective AR coating will severely reduce these beams' intensity compared to the primary reflections off the uncoated surface, rendering their effect on the captured fringe pattern negligible.

Pursuing this solution for the infrared system, a 0.5% antireflection coating was applied to one surface of the ZnSe window, a relatively standard specification for a ZnSe element at 45º incidence. It was observed, however, that the active and reference beams created using this element suffered from a low-contrast interference pattern which distorted the desired fringe pattern (Figure 2-9). The low-contrast pattern was traced to variations in the thickness of the beam splitter, hinting at the insufficiency of the specified 0.5% AR coating compared with the 28% reflectivity of the uncoated ZnSe surface. This was verified using Equations (2-3) and (2-4)

$$I_{\max} = I_{active} + I_{ref} + 2\sqrt{I_{active} I_{ref}} = 0.280 + 0.005 + 2\sqrt{0.280 * 0.005} = 0.360$$
$$I_{\min} = I_{active} + I_{ref} - 2\sqrt{I_{active} I_{ref}} = 0.280 + 0.005 - 2\sqrt{0.280 * 0.005} = 0.210$$

$$\Rightarrow \%\,\text{contrast} = \frac{0.360 - 0.210}{0.360} \times 100 = 41.6\%$$

The high fringe contrast predicted by this calculation verifies that the specified 0.5% AR coating was too relaxed, leaving reflections off the beam splitter's second surface with sufficient intensity to distort the primary beams. The coating could have been

improved to around 0.2% reflectivity. However, this still would not sufficiently reduce the contrast of the distorting thickness fringes. Moreover, any significant improvement beyond this would fall outside the bounds of conventional AR coatings for ZnSe optics and, therefore, become technically and financially impractical. Instead, the AR coating was removed and the beam splitter reground into a wedge shape to implement a classic trick also employed by Kwon, et al. in their Twyman-Green system [11]. The 1º angle between the wedge's two surfaces resulted in an angular separation between their respective reflections. Through proper tuning, the undesired reflections off the second surface could then be isolated and eliminated. This resulted in a significantly improved, distortion-free fringe pattern (Figure 2-10).

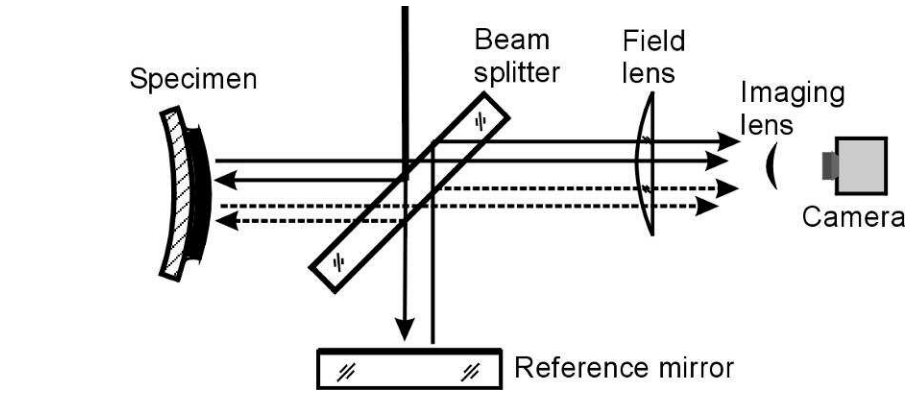

(a)

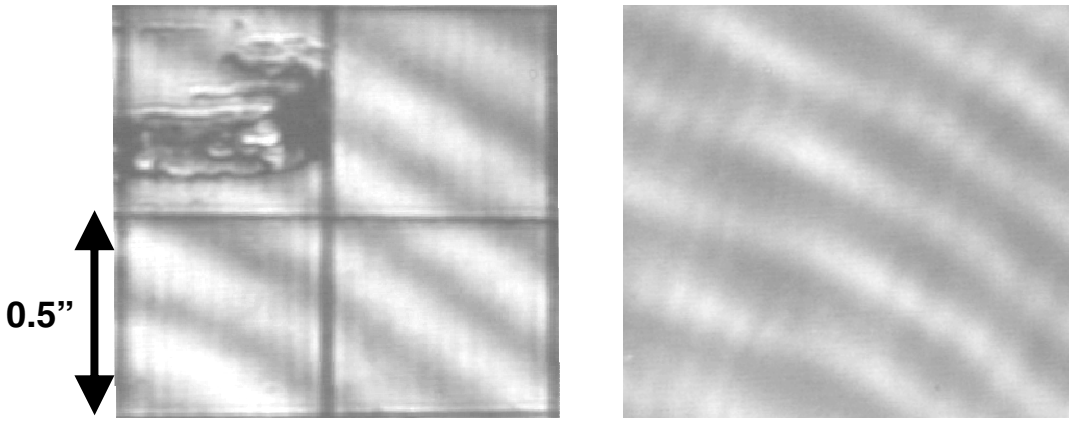

(b) (c)

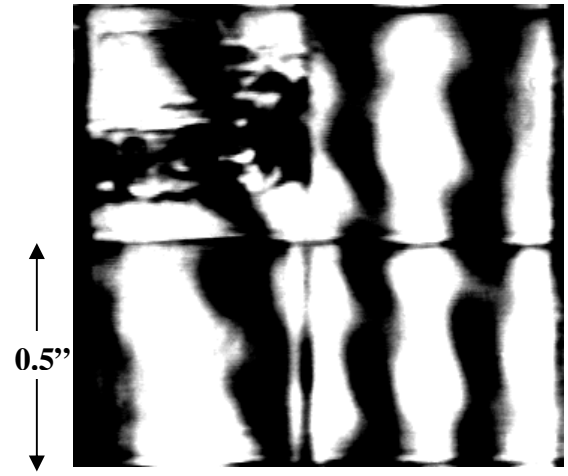

(d)

Figure 2-9(a): Beam paths using parallel-surface beam splitter; Example results show thickness fringes in the (b) specimen and (c) reference fields, resulting in (d) a distorted fringe pattern.

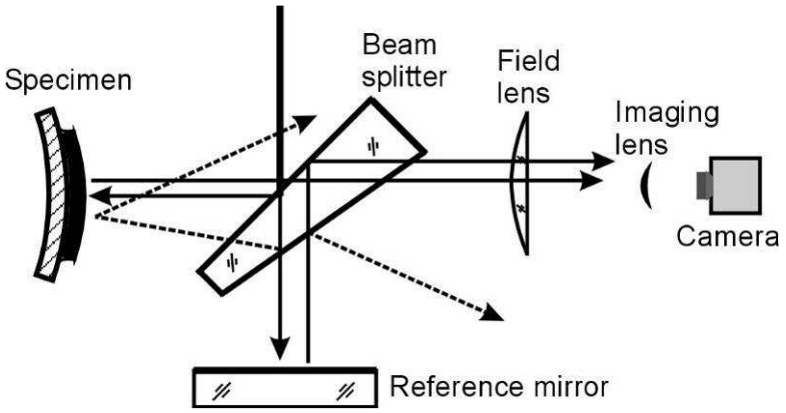

(a)

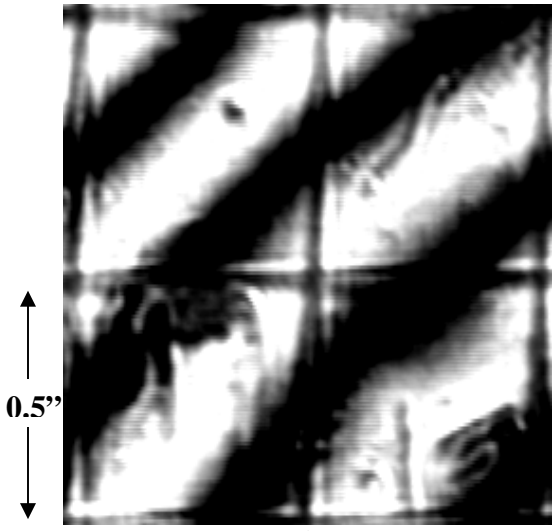

(b)

Figure 2-10(a): Wedge-shaped beam splitter design, resulting in (b) a distortion-free fringe pattern.

2.4.2 Implementation of Larger Field of View

The FITGI needed a $2\sqrt{2}$" beam diameter to attain the required 2" by 2" field of view. To accommodate this large beam, the oven windows, field lens, and collimating lens were all 3.5" in diameter; the beam splitter had a larger 4" diameter to account for the 45° angle of incidence on this element. This led to concerns over whether quality and uniformity could be maintained throughout these large elements. The quality of the beam splitter and oven windows was especially crucial given that these elements act on the active and reference beams separately. Whereas wavefront distortions from the field or collimating lenses affect both beams equally, distortions introduced into one beam by the beam splitter or oven windows is not compensated by an identical distortion of the other beam. In this case, the fringe pattern would no longer provide an accurate representation of the specimen's topography.

The optics' quality was tested by examining the null field using a known optical flat for the specimen. Because there were no surface variations between this specimen and the reference flat, a perfect system should produce a null field of uniform intensity. The null field produced by the FITGI, however, showed roughly 1.5 oval-shaped fringe over a 2.4" diameter optical flat (Figure 2-11), a problem that was isolated to the beam splitter by testing each element individually.

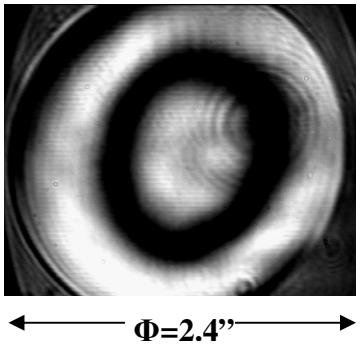

Figure 2-11: Null field distortion

Knowing that the beam splitter was inducing wavefront distortions, the question then became how to mitigate the effect on the interference pattern. As can be seen in Figure 2-10, using the ZnSe window's front surface as the beam splitter requires the active and reference beams to make one and three passes through the element, respectively. With a perfect optical element, the resulting difference of two passes through the beam splitter is not a problem. When using an imperfect element, however, each pass compounds another level of wavefront distortion. In the case where the front window surface is used for the beam splitter, bringing the active and reference beams together is therefore equivalent to interfering a flat wavefront with a beam which has suffered through two passes through the faulty beam splitter. The situation is not improved when using the window's back surface as the beam splitter; this only changes which beam suffers the more severe distortion.

Instead of using only one of the ZnSe window's surfaces, the FITGI employed a novel approach in which both surfaces are used for the beam splitter. As before, the front surface reflected the active beam. Instead of using this same surface for the reference beam, however, the tilt of the reference flat was adjusted to reflect the

reference beam from the back surface into the imaging system (Figure 2-12). In this case, both beams only pass through the troublesome element one time, resulting in no relative distortion. Retesting the null field verified that, while some distortion was still present, the magnitude had been significantly reduced (Figure 2-13). Further, that which remained was the result of distortions induced by the oven windows and other elements in addition to the beam splitter.

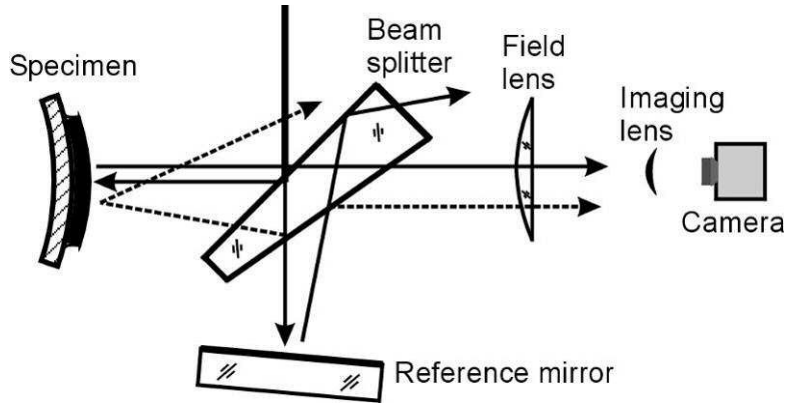

Figure 2-12: Beam splitter employing both window surfaces

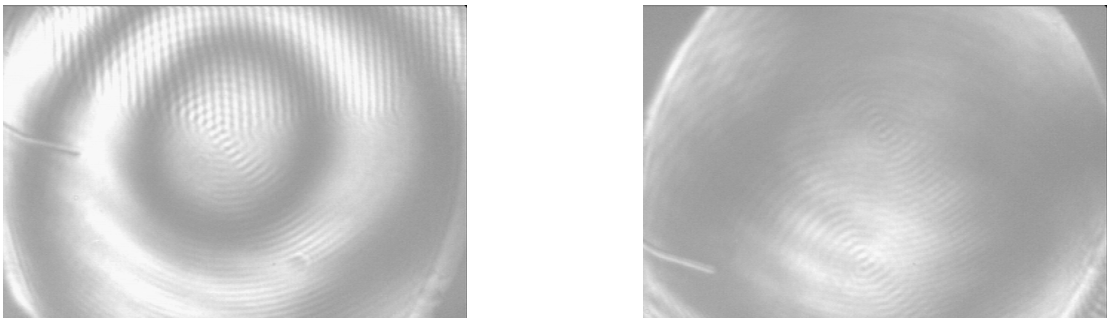

(a) (b)

Figure 2-13: Null field using (a) the same surface and (b) opposite surfaces of the beam splitter

The aforementioned solution sufficiently mitigated the effect of beam splitter-induced distortions on the interference pattern. However, the exact cause of the distortions remained in doubt.

Technically speaking, wavefront distortions result from variations in the optical path length (OPL) encountered by individual rays as they travel through space. When taking into account the 45° incidence on the beam splitter, the observed oval fringe shape indicated that the optical path length varied radially from the element's center. Since the optical path length is defined as [2]

$$OPL = \int_L n(x)dx \tag{2-8}$$

this could only be caused by radial variations in either the element's index of refraction *n(x)* or its thickness corresponding to the physical length *L*.

The beam splitter window's flatness was specified at 633 nm/inch. Therefore, over a 2" radius, the flatness could vary by 1266 nm, resulting in a maximum possible thickness variation of 2532 nm between the element's two surfaces. Knowing the 1.4 index of refraction difference between ZnSe (2.4) and air (1.0), two passes through such an element at 45° incidence would induce a distortion of approximately 10 μm, or roughly one fringe at λ = 10.6 μm. Assuming that the specified flatness was met, this could only account for about half of the wavefront distortion seen in Figure 2-11 and Figure 2-13(a). This case does illustrate an important point, however; the high index of refraction of ZnSe makes up for a significant portion of the flatness requirement relaxation afforded by infrared's long wavelength.

ZnSe elements are grown through a sensitive chemical vapor deposition (CVD) process [13]; therefore, a radial refractive index variation occurring as the element is grown seems plausible. Figure 2-14 illustrates a theoretical scenario where the index of refraction varies linearly through a difference of 0.005 between the center and edge for the ZnSe window's specified wedge geometry. A MATLAB simulation showed that such an element would induce wavefront distortions similar to those observed experimentally in the actual element (Figure 2-15). A rough calculation corroborates this model: a 0.005 refractive index difference applied over the beam splitter's average 2.25 mm thickness distorts the wavefront by 22.5 μm, or roughly two fringes at λ = 10.6 μm . As this calculation shows, the absolute thickness is also a crucial parameter in elements with a variable refractive index; thinner elements will create less distortion for the same amount of refractive index variation due to the shorter distance over which the wavefront is exposed to the variation.

It should be emphasized that the index of refraction model is only a hypothetical scenario driven by experimental observation. Therefore, the close agreement between simulation and experiment evident in Figure 2-15 does not eliminate flatness variations as a possible or even probable cause. A means of identifying the true cause is left for the discussion of future work in Chapter 5.

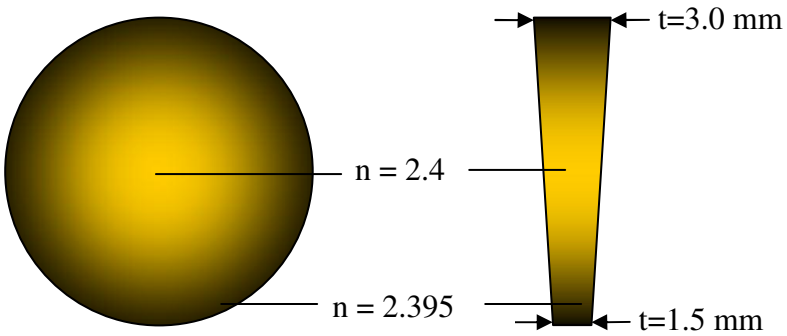

Figure 2-14: Front (*left*) and Side (*right*) views of the modeled beam splitter's geometry

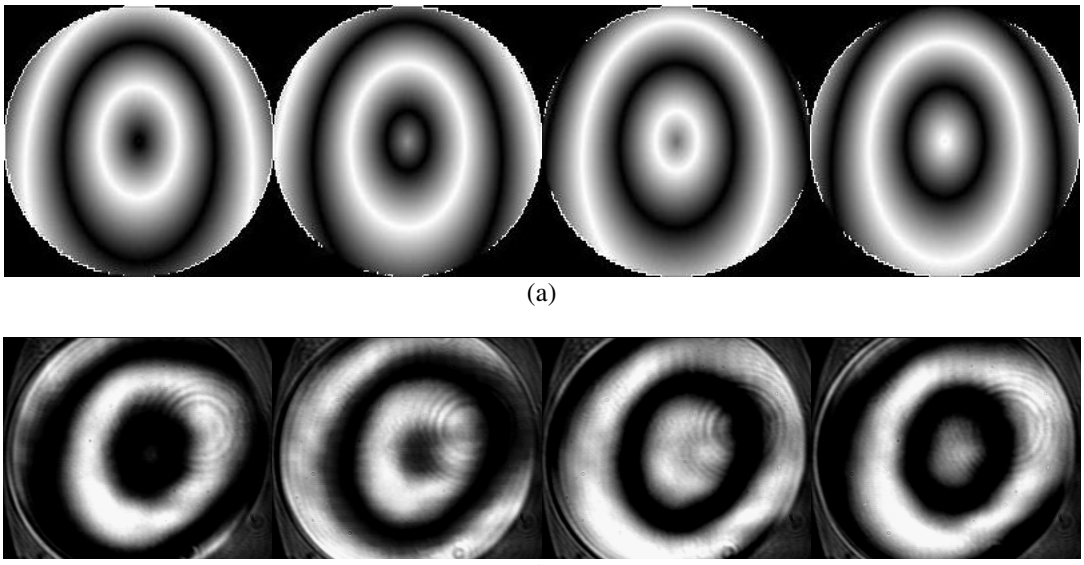

(a)

(b)

Figure 2-15: Phase-shifted sequence of (a) Simulation results compared with (b) Experimental results

Specimen Holder Design / System Stability

Using a simple horizontal plate as the system's specimen holder required that the specimen be viewed vertically; that is, looking down from the top of the oven. Such a design could have been implemented directly by locating the beam splitter above the oven and adding a viewing window to the top oven wall. However, concern over fringe instabilities induced by the varying refractive index of air currents rising off the oven at high temperatures made such a configuration impractical. Instead, a 45° mirror made it possible to view the specimen through the side oven wall. The mirror temporarily turned the beam vertical for specimen illumination (Figure 2-16). This *pseudo-vertical viewing* design made it possible to view a specimen held in a horizontal orientation while avoiding the problematic air currents above the oven.

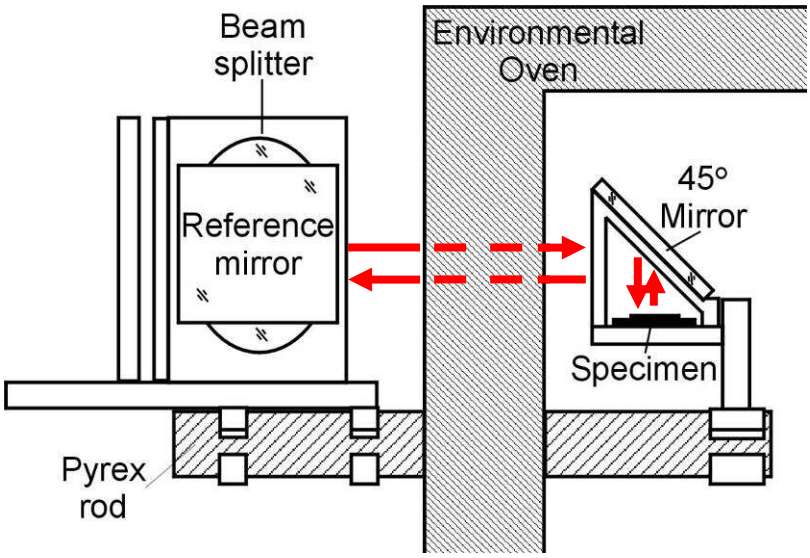

Figure 2-16: Pseudo-vertical viewing design. The red lines denote the optical path of the IR beam

The specimen holder was connected to an external base shelf via a 1.25" diameter Pyrex rod. The reference mirror and beam splitter were connected to this same shelf, creating a close mechanical connection. Any environmental vibrations were suffered simultaneously, minimizing relative motion between these three key elements. This minimized relative optical path length variations, thereby enhancing the stability of the system and diminishing the effect of oven vibrations.

2.5 Application: Warpage of Flip-Chip Package with Aluminum Stiffener

The completed FITGI was run through several representative experiments to test the system and demonstrate its capabilities. Figure 2-17 provides details on an experiment run on a flip-chip with an aluminum stiffener. This specimen was subjected to a temperature profile starting at room temperature, heating up to 220 °C after stopping briefly at 100 °C, down to 0 °C, and finally back to room temperature.

After the experiment, an in-house fringe analysis program was used to analyze the captured fringe patterns and create 3-D warpage maps (Figure 2-18). The deformation was also plotted along a diagonal through the center of the silicon chip (Figure 2-19). The results show that the silicon chip, which started the experiment concave down, flattened out around 100 °C, and had reversed concavity by 220 °C. As should be expected, cooling to 0 °C reverted the chip's concavity back to its original state. The aluminum stiffener went through this process backwards, beginning the experiment concave up, flattening out during heating, and turning

concave down by 220 °C. Interestingly, its concavity did not immediately return to its original state after cooling to 0 °C.

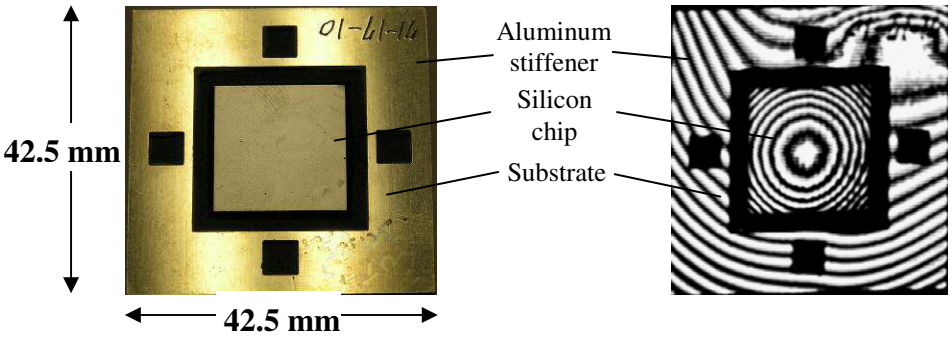

(a) (b)

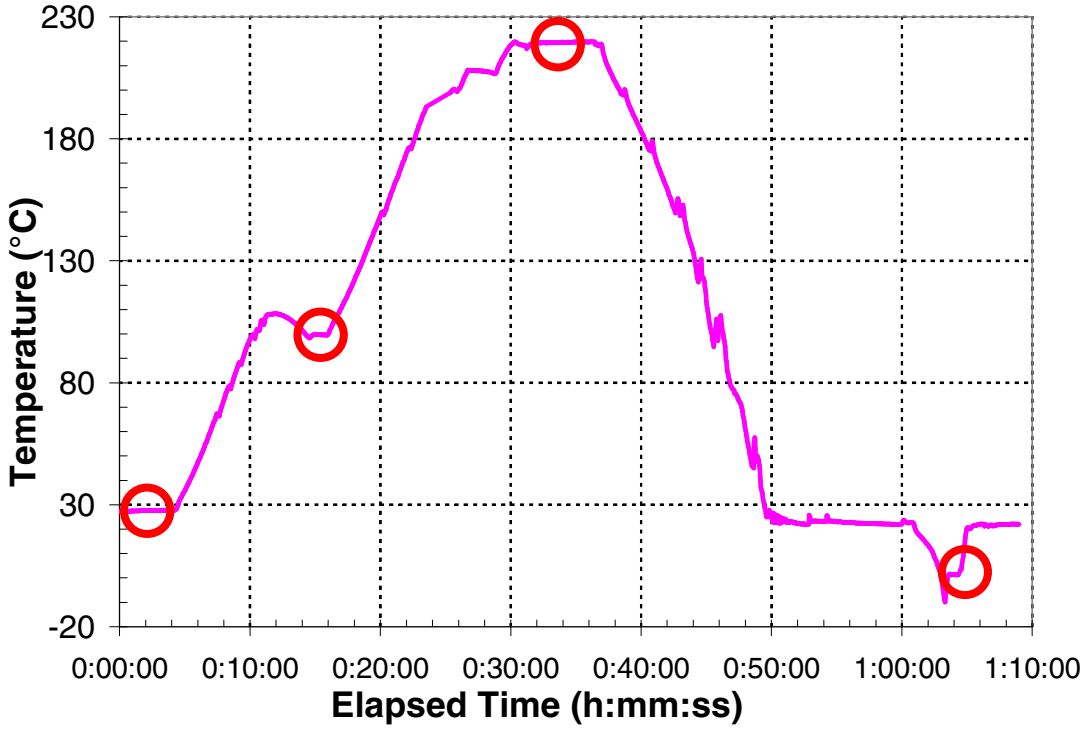

(c)

Figure 2-17(a): Specimen under visible illumination. Note the low specularity of the silicon chip compared with the aluminum stiffener, (b) Fringe pattern from the IR interferometer, (c) Temperature profile followed during experiment.

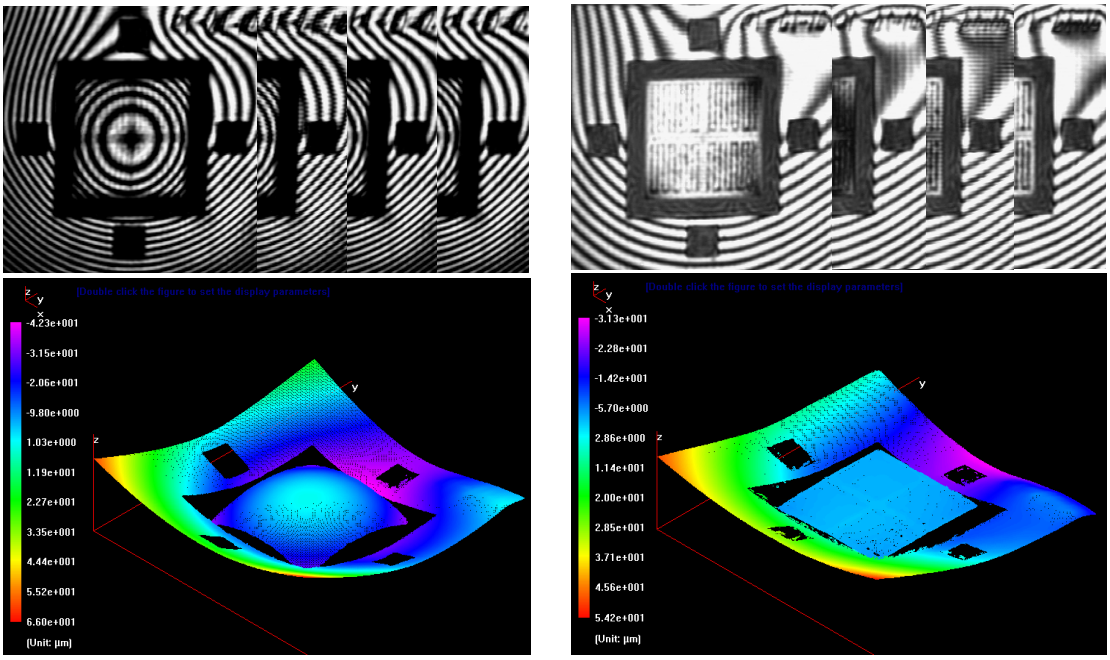

(a) 22 °C (b) 100 °C

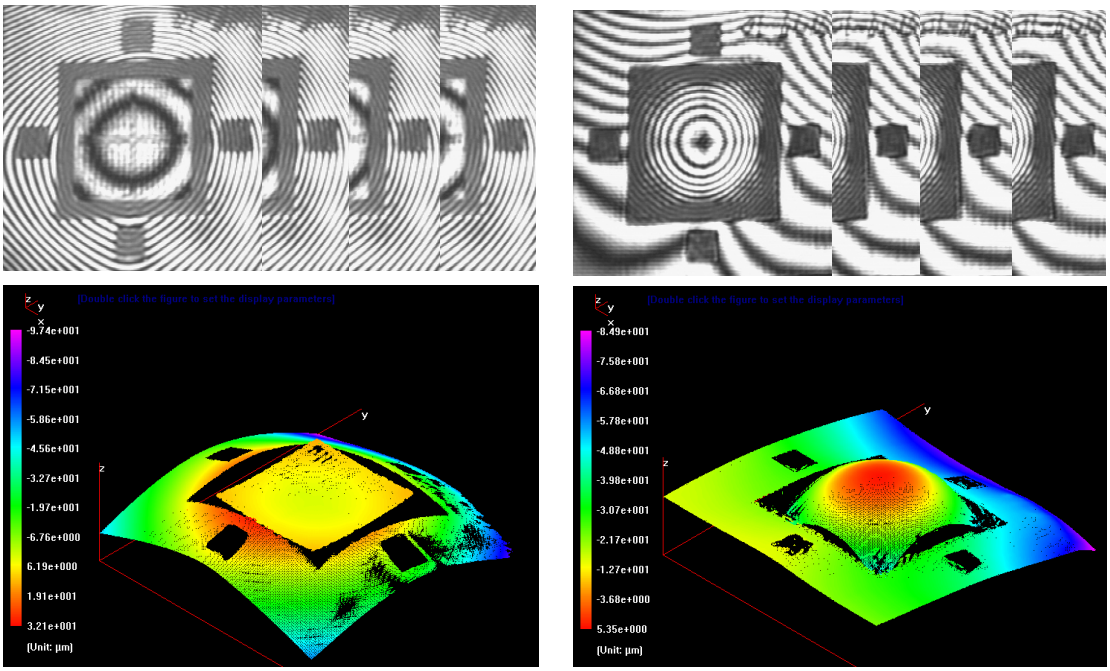

(c) 220 °C (d) 0 °C

Figure 2-18: Fringe patterns (top) and 3-D maps (bottom) measured during the FITGI experiment

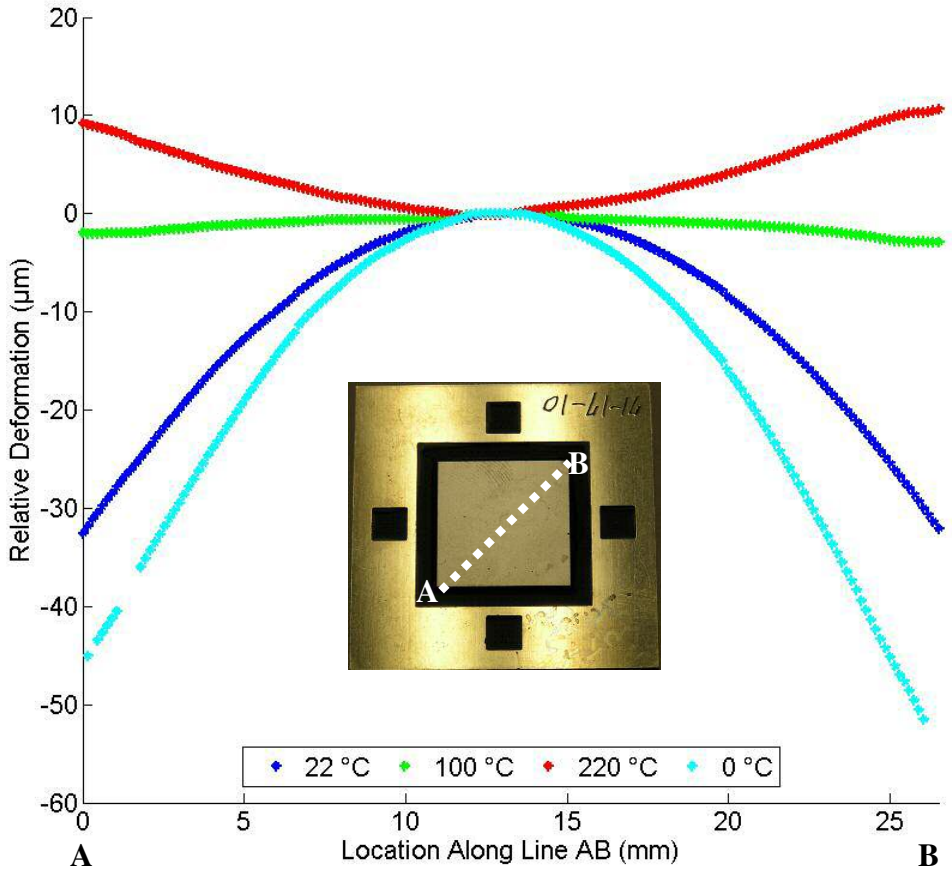

Figure 2-19: Deformation of the silicon chip along line AB

CHAPTER 3: SHADOW MOIRÉ WITH NONZERO TALBOT DISTANCE

3.1 Background and Motivation

3.1.1 Technical Review: Shadow Moiré

Shadow moiré is a popular out-of-plane measurement technique wherein a reference grating with alternating opaque bars and transparent spaces is placed in close proximately to the specimen's surface (Figure 3-1). A light source projects the grating lines as shadows on the specimen's surface. The shape of the shadows is a function of the topography of the surface. The interaction between the grating lines and the projected shadows produces a moiré effect that is captured by a camera. To ensure good diffusivity and high visibility shadows, the specimen surface is coated with a thin layer of matte white paint [4].

The governing equation for shadow moiré is given by [2]

$$z(x, y) = \frac{g}{\tan\alpha + \tan\beta} N(x, y) \tag{3-1}$$

where $z(x,y)$ is the specimen-to-grating distance, g is the pitch of the reference grating, $N(x,y)$ is the fringe order, and α and β are the angles of illumination and observation, respectively. In the general case, the specimen-to-grating distance z is not directly proportional to the fringe order N due to variations in the angles α and β with the x-coordinate. To deal with this, the light source and imaging system are often placed at the same distance L from the plane of the specimen. Assuming

negligible variability in z compared to L, $\tan \alpha + \tan \beta$ is then constant for all x, providing a constant contour interval over the entire field of view.

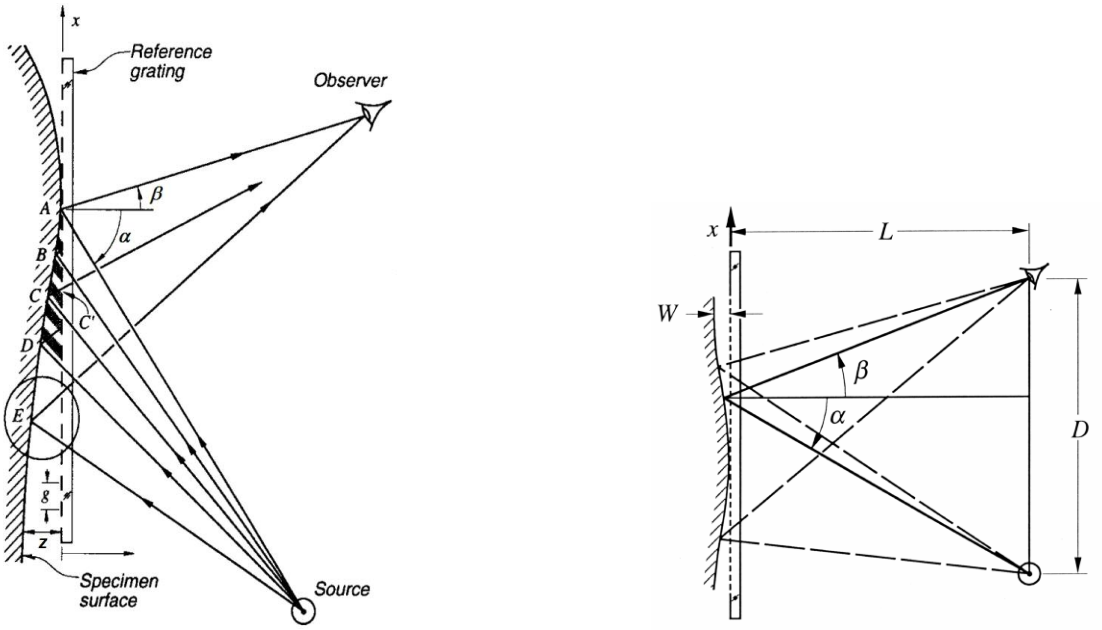

(a) (b)

Figure 3-1(a): Shadow moiré technique [2] and (b) configuration for constant contour interval [2]

3.1.2 Technical Review: Talbot Distance

Conventional practice of shadow moiré assumes that light propagates rectilinearly as depicted in Figure 3-1. While valid for reference gratings with a broad pitch, this assumption breaks down with the emergence of diffractive effects in finer gratings. In the latter case, the closely spaced reference grating lines induce a diffraction grating self-imaging phenomenon known as the Talbot effect [14] wherein interference between diffracted beams creates virtual images of the grating that produced them. The resulting virtual gratings are located at regular intervals behind

the real grating (Figure 3-2). The distance between successive virtual gratings is called the Talbot distance, D_T^α, which for inclined illumination is given by [15]

$$D_T^\alpha = \frac{2g^2}{\lambda}\cos^3\alpha \tag{3-2}$$

where λ is the wavelength of light, g is the pitch of the reference grating, and α is the angle of illumination.

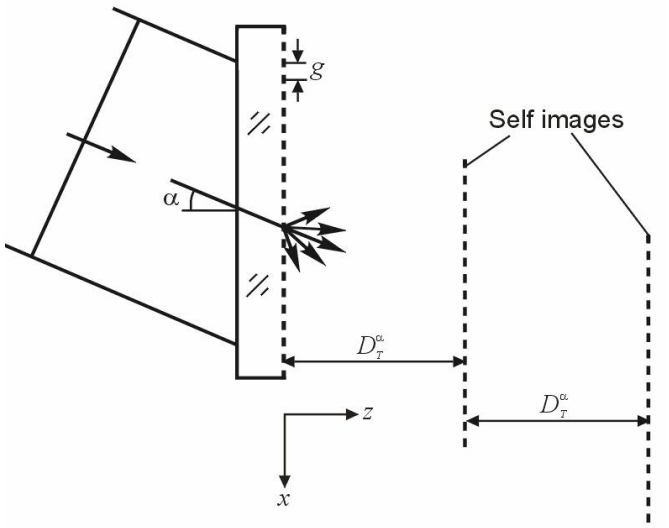

Figure 3-2: Talbot effect for inclined illumination (*modified from* [4])

In addition to the virtual diffraction gratings at mD_T^α, the Talbot effect produces virtual images of the diffraction grating's complement at odd multiples of $D_T^\alpha/2$. In between these two sets of high contrast virtual gratings (i.e., at odd multiples of $D_T^\alpha/4$) are washout regions, constant intensity fields devoid of grating lines (Figure 3-3).

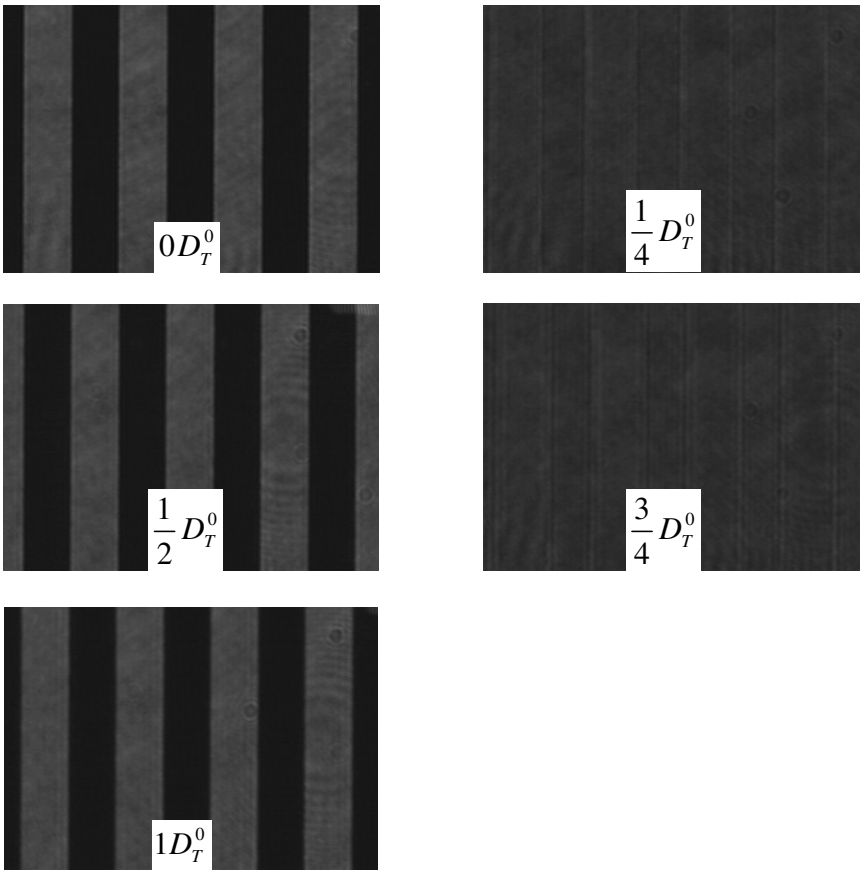

Figure 3-3: Virtual images produced by the Talbot effect at distances $mD_T^0/4$ (α=0) [16]

3.1.3 Prior Work: Shadow Moiré at Nonzero Talbot Distances

Conventional shadow moiré operates in the zeroth Talbot region immediately behind the reference grating. This practice works fine for low-sensitivity applications employing broad reference gratings with long Talbot distances but breaks down for fine reference gratings used to achieve higher sensitivities. While the contour interval decreases with g per (3-1), D_T^α decreases with g^2 per (3-2), resulting in an increasingly small zone of high contrast fringes between the grating and the washout region at $D_T^\alpha/4$. This limits the dynamic range in which high contrast moiré fringes

can be achieved, resulting in fringe contrast loss when measuring specimens with excessive deformation or non-coplanar surfaces (Figure 3-4) [4]. The required proximity between the specimen and reference grating also increases the likelihood for contact during phase shifting.

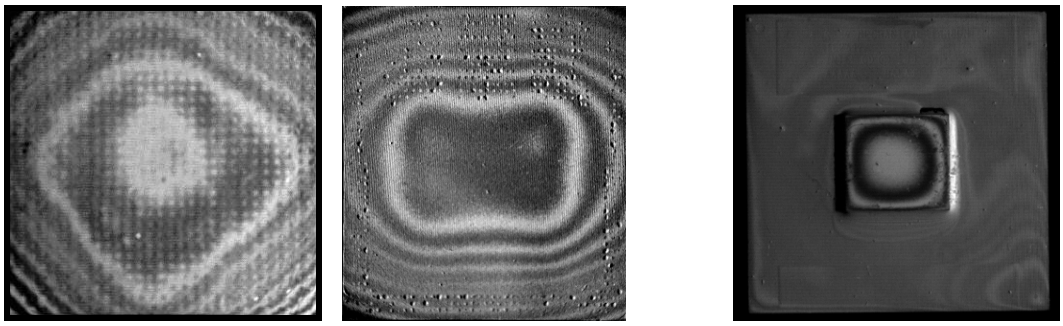

(a) (b)

Figure 3-4: Limitations of conventional high-sensitivity shadow moiré include (a) excessive deformations, and (b) non-coplanar surfaces [4]

Given these inherent drawbacks to high-sensitivity systems using fine-pitched reference gratings, it is tempting to turn to an image processing technique such as phase shifting to enhance the basic sensitivity of low-sensitivity systems employing broad reference gratings. While such techniques have been previously employed with shadow moiré, it has been assumed that the fringe patterns' intensity varies sinusoidally per (1-1) as it does in the case of two-beam interference [4,5,17-20]. In actuality, the intensity distribution of shadow moiré fringes is much more complicated. Therefore, the ability of phase shifting to enhance a low sensitivity shadow moiré configuration is fundamentally limited by systematic errors introduced by the sinusoidal intensity distribution assumption [4,17].

To overcome these difficulties, Wei, et al. attempted to propose a new shadow moiré technique that uses a fine-pitched reference grating but places the specimen at the virtual reference grating at the half Talbot distance ($D_T^{\alpha}/2$) [21]. Operating in this region creates more distance between the specimen and reference flat, allowing for an enhanced dynamic range and eliminating the impracticalities associated with conventional high-sensitivity shadow moiré using fine reference gratings. Despite its contribution, the study by Wei, et al. was misleading in its handling of the effect of inclined illumination and diffraction.

The design of experiments for effective measurements at the nonzero Talbot distance requires detailed knowledge of the fringe intensity and contrast as a function of the distance between the specimen and reference grating. A comprehensive theoretical analysis by Han, et al. showed that, when using the nonzero Talbot distance, fringe pattern contrast is affected by two factors: the Talbot effect and the aperture of the imaging system [4,22]. Because the former is a function of the source's wavelength per (3-2), the spectral bandwidth of illumination also plays a role, causing a reduction in the contrast for higher Talbot distances (Figure 3-5).

Figure 3-6 illustrates the aperture effect wherein the finite aperture d admits light to the imaging system from a location where the mismatch of the reference and shadow gratings should produce a dark fringe, lowering the contrast of the shadow moiré pattern [4,22-24]. It has been shown that the influence of this effect increases with the specimen-to-grating distance z and the effective aperture d_e, where the latter is

defined as the ratio between the aperture d and the distance between the aperture and the reference grating L ($d_e = d/L$) [4,22]. It is also inversely proportional to the grating pitch, g.

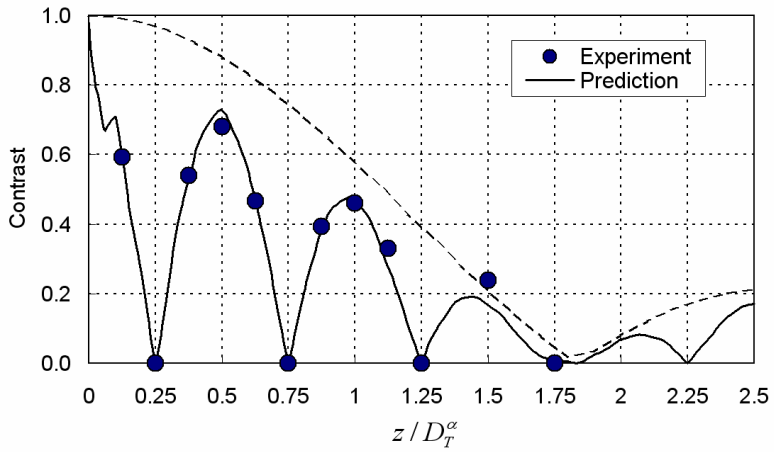

Figure 3-5: Contrast at normalized specimen-to-grating distances z assuming a pinhole aperture. The dashed line indicates the limit imposed by the spectral bandwidth of illumination ($\Delta\lambda \approx 300$ nm, $\lambda \approx 550$ nm) [22]

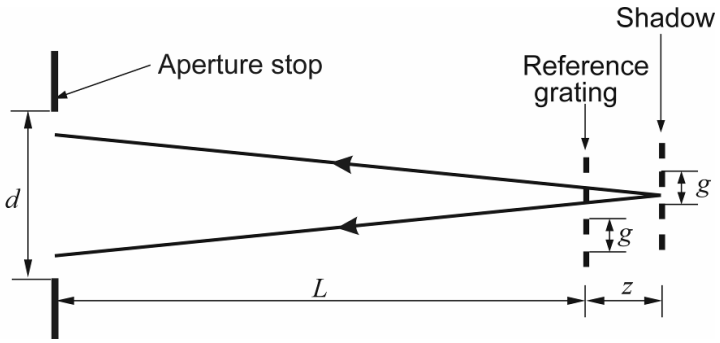

Figure 3-6: Finite aperture admits undesired light, lowering the contrast of the fringe pattern [4]

Figure 3-7 summarizes the conclusions drawn by Han, et al. Requiring that the shadow moiré configuration meet certain practical criteria, the authors found that

conventional shadow moiré was practical down to a contour interval of approximately 110 µm. Using the nonzero Talbot distance extended this useful range down to approximately 43 µm. Further, Han, et al. recommended that a shadow moiré configuration with an angle of incidence $\alpha = 63°$ and an effective aperture $d_e = 0.01$ was ideally suited for working outside the zero Talbot distance [4,22]. The authors felt that this configuration provided the best combination of high sensitivity, large dynamic range (i.e., Talbot distance), and high fringe contrast at the half Talbot distance after accounting for the spectral bandwidth and aperture effects. As will be seen, this advice provided the foundation for the SMNT design.

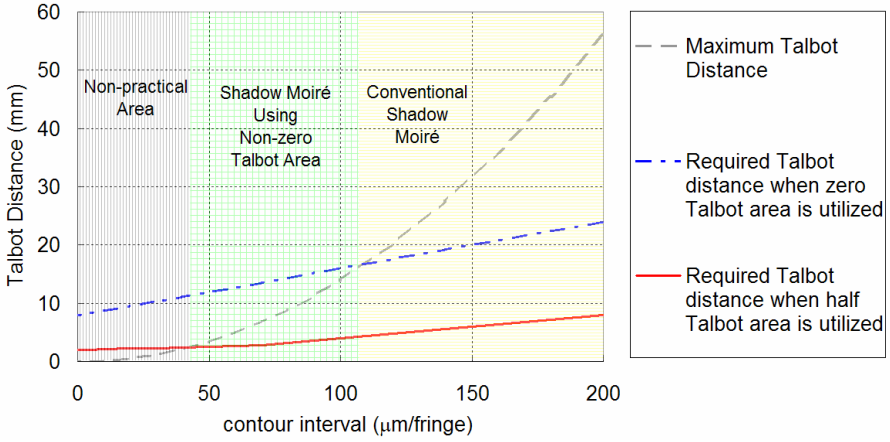

Figure 3-7: Sensitivity range of conventional and non-zero Talbot distance shadow moiré [4,22]

3.2 Design Requirements

To make the system suitable for testing a variety of specimens, the field of view provided by SMNT had to be adjustable and accommodate a range of sizes between 0.5" by 0.5" and 4.0" by 4.0". As with the FITGI, the implemented specimen holder also had to allow the specimen to deform freely. The holder used in the SMNT

supported the specimen at exactly three points with the intention of minimizing the rigid body motion incurred during deformation (Figure 3-8). The holder design also incorporated a means of tuning the specimen's tilt using a set of adjustment screws. While this was suitable for the initial setup, the screws were inaccessibly located inside the oven during experimentation. Therefore, the SMNT also had to incorporate an external tilting apparatus to provide adjustability during thermal cycling.

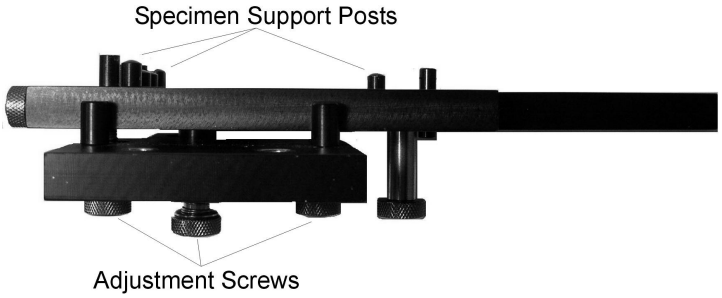

Figure 3-8: SMNT specimen holder

3.3 Final Design Overview

3.3.1 Mechanical Configuration

Required hardware for the SMNT included a light source for illumination, a camera for image capture, a translation system for phase shifting, and an environmental oven for thermal cycling. These components were connected to a personal computer (Figure 3-9), which coordinated their operation using the same LabView control program used with the FITGI system.

The light source consisted of a slit aperture illuminator head connected to a Dolan-Jenner model DC-950 150W illumination box through an optical fiber. The intensity

out of the illumination box could be controlled locally using a knob on the front of the box or remotely through a serial connection to the control computer.

A Pulnix TM-72EX 2/3" format black and white CCD camera was used in conjunction with the Pulnix SV5 frame grabber to capture and display the shadow moiré patterns on the control computer. The excellent stability of the system's fringe patterns allowed the camera to be set to its slowest shutter speed (1/60 second). This maximized the intensity striking the sensor, thereby maximizing the signal-to-noise ratio in the captured fringe patterns.

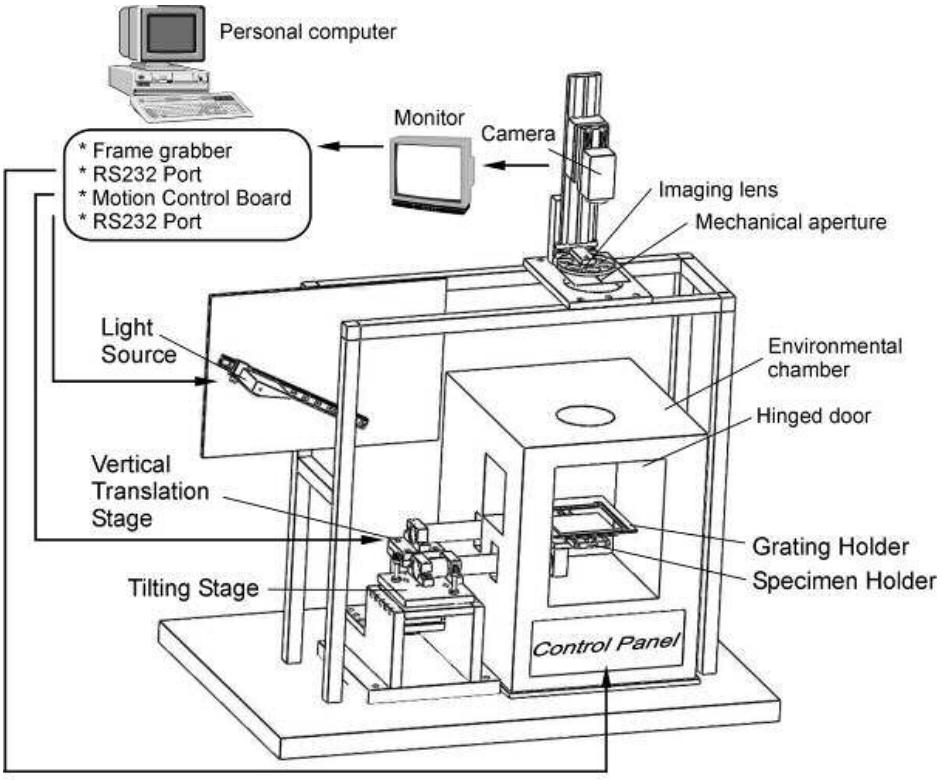

Figure 3-9: SMNT mechanical configuration

The phase shifting mechanism was composed of a J.A. Noll model NPZ-1/2 half-inch vertical translation stage driven by a Thorlabs Z625B one-inch motorized actuator. The grating holder was mechanically connected to this translation assembly, allowing the grating to move in relation to a fixed specimen. The specimen holder was independently connected to an external tilting assembly, providing the necessary means of adjusting the fringe pattern during thermal cycling. Except for its range of motion, the Z625B was the same as the Z612B used in the FITGI system; therefore, one Thorlabs DCX-PCI100 board controlled phase shifting in both systems.

The convection chamber was the same Sun model EC1A used in the FITGI system. A 4.0" wide by 4.5" tall rectangular port in the side wall and a 4.0" diameter port in the top wall held double-paned windows for illuminating and viewing the specimen, respectively. In addition, two smaller 1.7" wide by 2.3" high rectangular ports in the side wall provided through-holes for connecting the specimen and grating holders to the external tilting and translation stages, respectively.

3.3.2 Optical Configuration

The imaging system was designed to maximize the contrast of the captured fringe pattern by taking full advantage of the theoretical work by Han, et al. A standard telescopic zoom lens could have accommodated a wide range of field of views and would have been easy to implement. However, the aperture in these devices is located behind a series of lenses. The study into the aperture effect by Han, et al., on the other hand, requires that the aperture be placed in front of any lenses. Therefore,

the imaging system was simplified to a circular aperture positioned in front of a single planoconvex imaging lens.

To maximize the usage of available intensity from the illuminator head, it was desirable to bring the illumination and imaging systems as close to the specimen's surface as possible. However, practical limitations on the lens-to-camera distance in the imaging system made it impossible to image fields of view as large as 4.0" unless the imaging lens was at least 11.5" from the specimen. This results from the equation for lens magnification

$$M = \frac{B}{A} \tag{3-3}$$

where M is the magnification, and A and B are the distances between the object plane and lens, and lens and imaging plane, respectively. Given that the sensor on a 2/3" format camera measures 6.6 mm in the shortest dimension and assuming that it is impractical to bring a lens within 0.75" of this sensor element, it is trivial to compute the shortest distance A capable of providing a 4.0" field of view:

$$\frac{6.6 \text{ mm}}{25.4 \frac{\text{mm}}{\text{in}} * 4.0 \text{ in}} = \frac{0.75 \text{ in}}{A} \Rightarrow A = 11.5 \text{ in}$$

The limited availability of focal lengths forced the final aperture position out to approximately 12.25" from the plane of the grating. It was also positioned for normal viewing ($\beta = 0$) to avoid angular viewing distortions.

A lens wheel stocked with a selection of imaging lenses provided a range of fields of view (Figure 3-10). The camera was positioned behind the lens wheel on a rack-and-

pinion track to accommodate the lenses' varying focal lengths. After positioning the proper imaging lens in the imaging position behind the aperture, the camera's position on the track was adjusted to obtain a sharp focus on the specimen. Table 3-1 lists the focal lengths and approximate lens-to-camera distances required to obtain various fields of view.

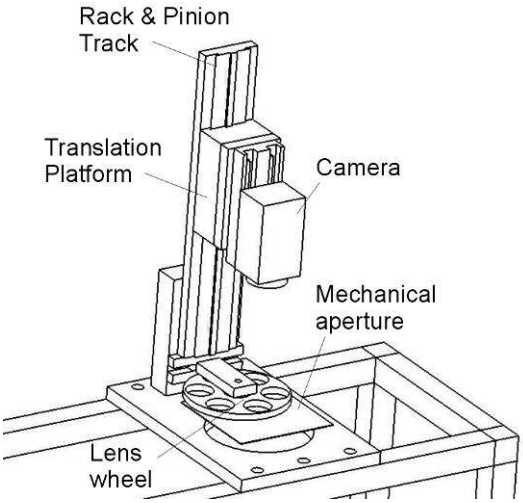

Figure 3-10: SMNT imaging system

Focal Length (mm)	Lens-to-Camera Distance (in)	Resultant Field of View (in)
19	0.8	3.9
25	1.1	2.9
35	1.6	2
50	2.3	1.3
75	3.9	0.8
100	5.9	0.5

Table 3-1: SMNT imaging system configuration for select fields of view

A black cloth bag draped over the top and sides of the imaging assembly blocked out stray light that would degrade the contrast of the captured fringe pattern. The bag was open at the bottom to admit light from the viewing window in the top of the oven. Zippered openings in the sides provided access to the lens wheel and camera translation platform.

Proportionality between fringe order and displacement was ensured by placing the illuminator head and aperture at the same L = 12.25" distance from the plane of the

grating. To achieve the $\alpha = 63°$ angle of illumination recommended by Han, et al., the illuminator was located at D = 24.50" from the aperture. Given the normal viewing of the imaging system ($\beta = 0$), this set the system's contour interval at half of the grating's pitch per (3-1). That is,

$$z(x, y) = \frac{g}{2} N(x, y) \tag{3-4}$$

3.4 Technical Challenges

Ideally, the imaging system's aperture should be kept as small as possible to minimize the configuration's effective aperture and thereby mitigate the reduction in contrast due to the aperture effect. Practically, however, smaller apertures come at the cost of a reduction in the intensity captured by the camera and a resultant decrease in the signal-to-noise ratio. Therefore, the aperture size had to be optimized to find a good compromise that admitted sufficient intensity while maximizing the fringe pattern contrast. To this end, a range of aperture sizes between 0.05" and 0.25" in increments of 0.05" were tested in the system. Based on the results, it was decided that a 0.15" aperture provided the best compromise between contrast and admitted intensity throughout the required field of view range. Interestingly, the effective aperture in this case was d_e = 0.15"/12.25" = 0.0122, which is nearly equal to the d_e = 0.01 recommended by Han, et al. It should be further noted that the most suitable aperture was dependent on the field of view. Therefore, the system was provided with the full range of tested aperture sizes. This made it possible to implement

smaller apertures with larger fields of view to maximize contrast and larger apertures with smaller fields of view to admit sufficient intensity.

3.5 Application: Warpage of Flip-Chip Plastic Ball Grid Array Package

As with the FITGI, the completed SMNT was tested in several representative experiments. Figure 3-11 provides details on an experiment run on a flip-chip plastic ball grid array package using a 5 lines/mm reference grating (g = 0.2 mm). The specimen was placed at the half Talbot distance; note the contrast uniformity over the entire field despite the significant amount of warpage.

The specimen was subjected to a temperature profile that started and ended at room temperature with an intermediate excursion to 255 °C. Figure 3-12 shows the resulting fringe patterns and 3-D warpage maps while Figure 3-13 shows a plot of the deformation about a diagonal through the specimen's center. The package started severely warped concave up, flattened out around 100 ºC, and had turned slightly concave down by 255 ºC. It returned to its original condition after cooling to room temperature (not shown). It should also be noted that the protruding bump that developed at higher temperatures was an air bubble trapped underneath the paint layer and not the result of localized deformation in that region.

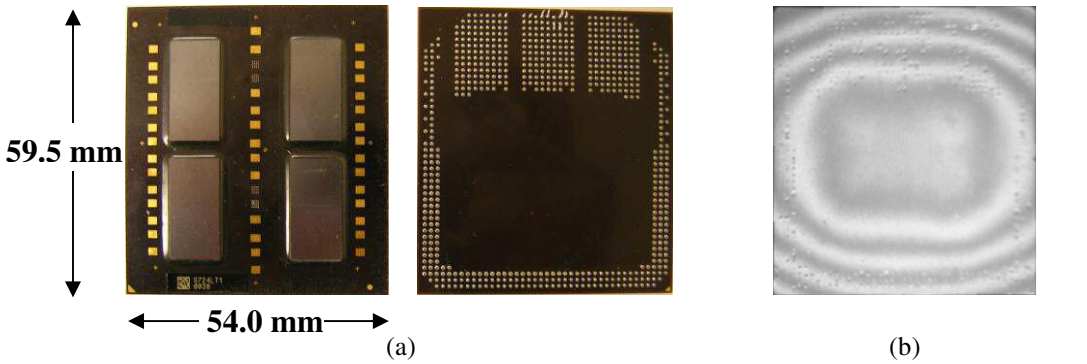

(a) (b)

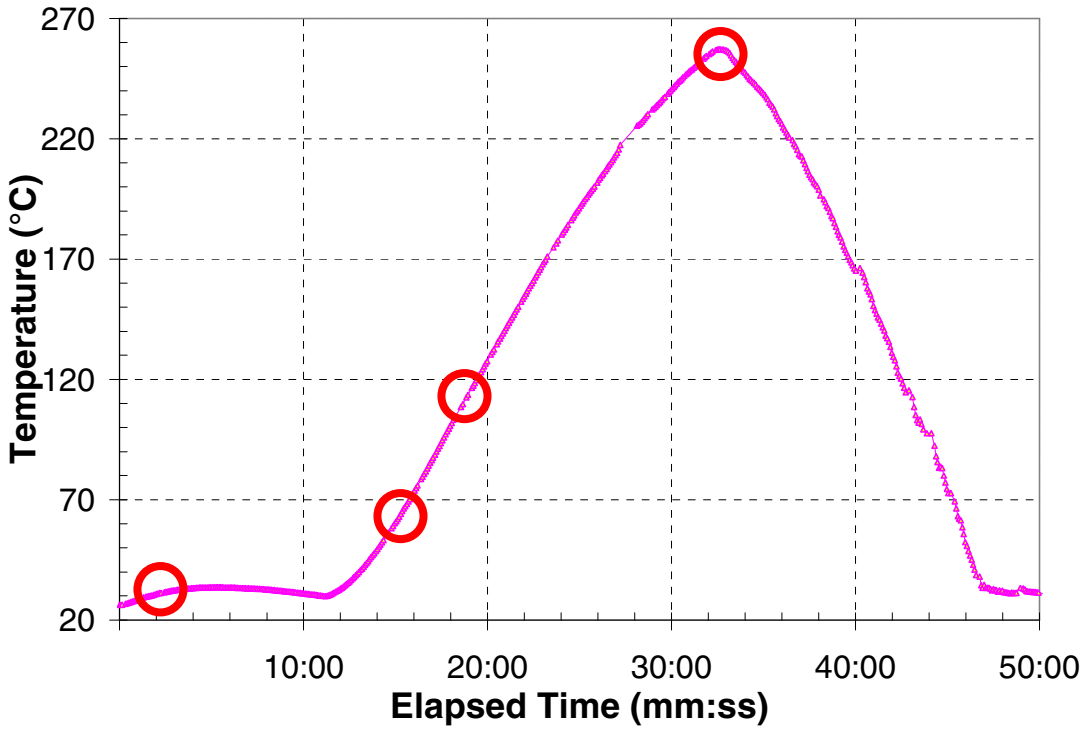

(c)

Figure 3-11(a) Specimen front (*left*) and back (*right*), (b) Fringe pattern of the back surface from the SMNT, (c) Temperature profile followed during experiment.

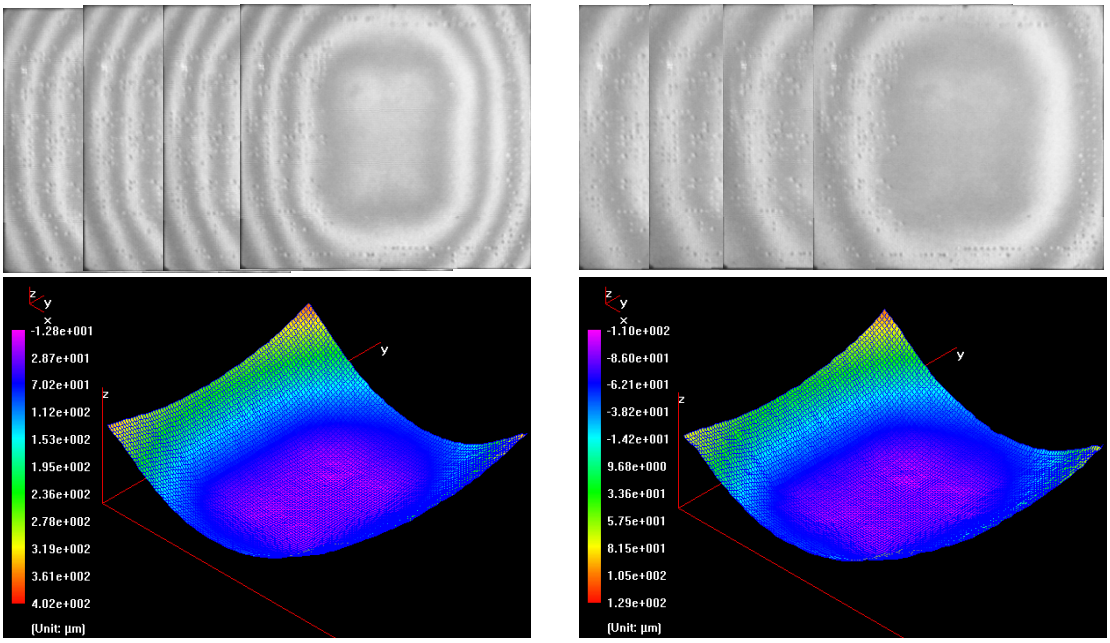

(a) 22°C (b) 56°C

(c) 109°C (d) 256°C

Figure 3-12: Fringe patterns (top) and 3-D maps (bottom) measured during the SMNT experiment

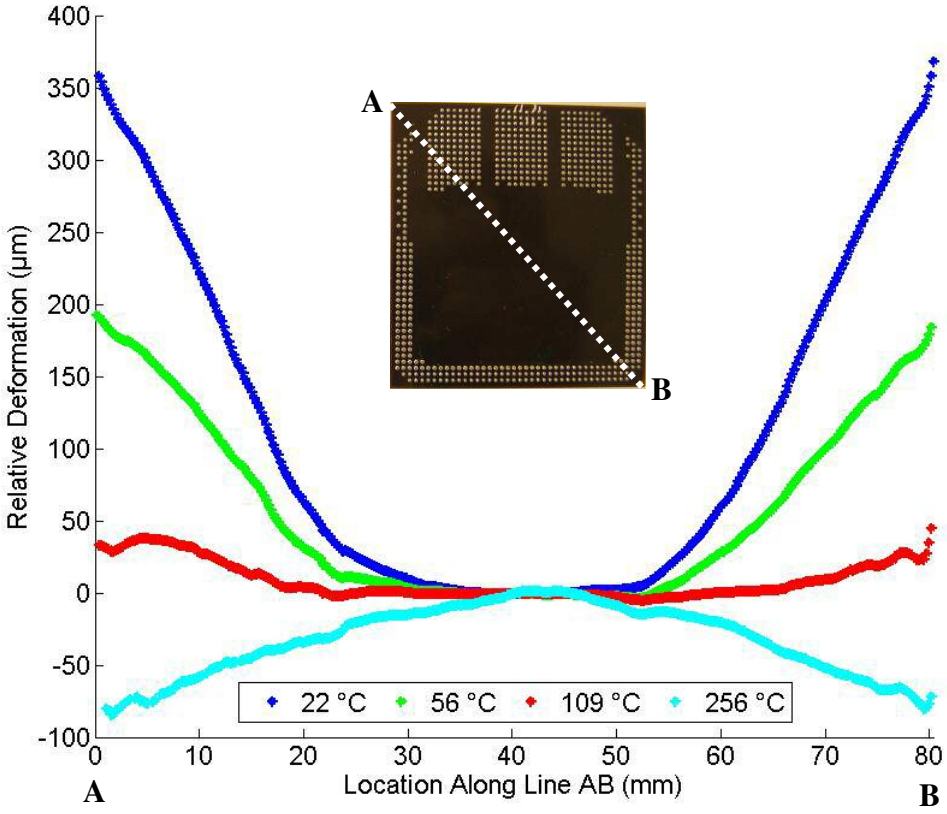

Figure 3-13: Deformation of specimen along line AB

CHAPTER 4: SOFTWARE

The SMNT and FITGI systems were controlled using a custom LabView-based program. Besides providing the user with a consolidated interface for monitoring and controlling the hardware (Figure 4-1), the program worked in conjunction with an independent fringe analysis program to create automatic real-time 3-D previews of the specimen's deformation (Figure 4-2). This provided the user with an idea of the extent and shape of the documented deformation even before the captured fringe patterns were run through more accurate post-experiment analyses.

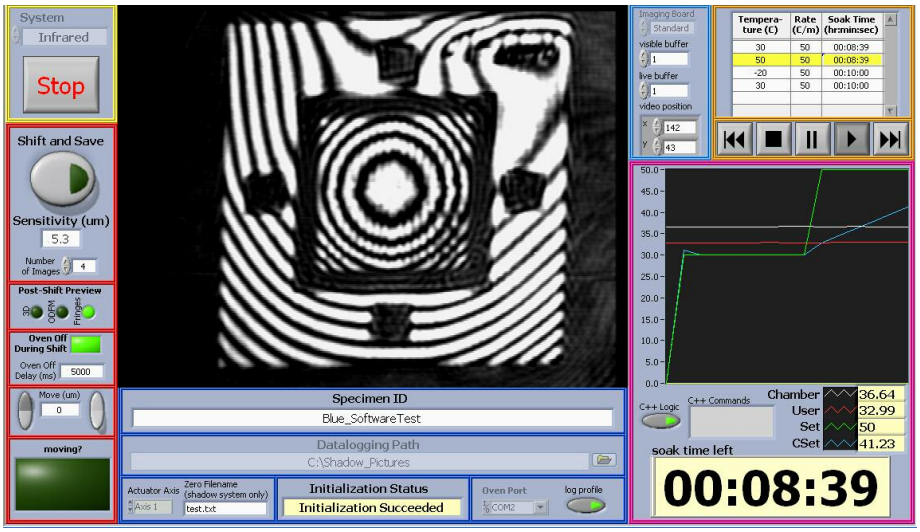

Figure 4-1: Control software's user interface

The software monitored and controlled the oven's status and settings through an RS-232 connection. The user could change the observed temperature profile at any time by entering the desired set points, ramp rates, and dwell times into a table on the front panel. Progress was updated every two seconds by querying the oven for the time left in the current dwell and the temperature of its two integrated thermocouples. In

addition to being displayed on the user's panel, the temperature points were also logged to a file for later reference.

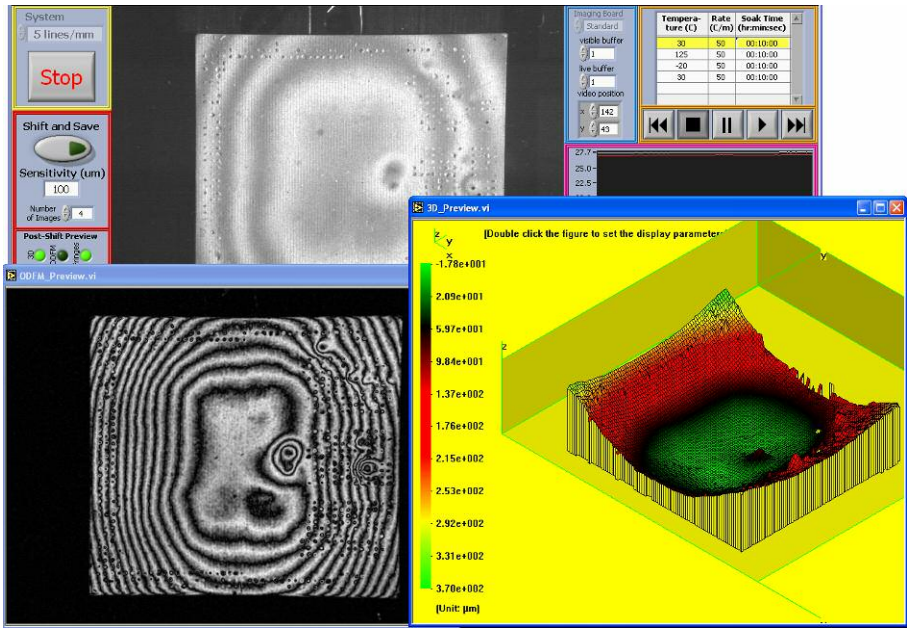

Figure 4-2: ODFM and 3-D preview of captured fringe patterns

Video streamed from the Pulnix imaging board to the application's main panel, showing live fringe patterns from the system. Image capture was coordinated with actuator motion to capture and save a series of phase-shifted fringe patterns for later analysis. The program could also be configured to automatically capture fringe sets in regularly spaced time intervals specified by the user. Images were saved in a user-specified directory with a filename composed of the specimen's name, the time, the current temperature, and the image's position in the current phase-shifted sequence. To minimize vibrations, the user had the option to turn the oven off during image capture; afterwards, the program turned the oven back on and resumed where it left off in the temperature profile.

CHAPTER 5: FUTURE WORK

The most pressing question hanging over the FITGI system was the source of the wavefront distortion seen as circular fringes in the system's null field. This can be resolved by testing the flatness of the ZnSe element's two surfaces using a traditional visible interferometer. This will quantify the thickness variations, making it possible to then indirectly quantify what, if any, index of refraction variations are present inside the element.

Several ideas have been suggested for further improving the nonzero Talbot distance system. For example, it has been proposed that the light source be moved closer to the grating plane when testing small specimen's to increase the available intensity from small fields of view. In this case, the angle of illumination will be held constant, only the distance between the grating and illuminator will change. While this will result in a variable contour interval per (3-1), the variation will become negligible when the field of view is sufficiently small. Additional advantages may be gleaned from using reference gratings with non-unity bar-to-space ratios. These ideas could not be implemented into the SMNT system but warrant further exploration as possible means of improving future SMNT iterations.

CHAPTER 6: CONCLUSIONS

Two advanced measurement systems were developed for characterizing out-of-plane displacements in microelectronic devices during thermal cycling. The first, a far infrared Twyman-Green interferometer, was described in Chapter 2. This system implemented a CO_2 laser's long wavelength to increase the specularity of rough surfaces which are too diffusive for traditional visible interferometers. The need for Twyman-Green given existing Fizeau systems was justified based on the former's physical separation of the active and reference paths. This made it possible to keep all optical elements outside the environmental oven, thereby enabling larger fields of view and enhanced fringe stability. Difficulties encountered during implementation were also described, including an effective beam splitter design and quality issues with the larger optical components. Possible explanations for observed wavefront distortions induced by these elements were presented and analyzed.

Chapter 3 described the implementation of a novel shadow moiré approach where the specimen is placed at the half Talbot distance. The need for this system was justified based on the limited dynamic range of conventional high sensitivity shadow moiré systems and the systematic errors introduced by phase shifting used to enhance low-sensitivity configurations. The system's simplified imaging system was described and justified. Optimization of the size of the imaging aperture was also discussed based on the tradeoff between intensity and fringe contrast.

Example experimental results were also presented, illustrating both systems' unique measurement capabilities.

While noting the aforementioned technical advantages over existing implementations, it is important not to overlook the value of the broad sensitivity range encompassed by the described systems. The infrared system provides a basic sensitivity of 5.3 μm while working at the nonzero Talbot distance makes it possible for the shadow moiré system to achieve sensitivities of 50-100 μm depending on the chosen reference grating. Assuming a practical ten-fold enhancement via the phase shifting method, these techniques therefore encompass a sensitivity range of approximately 0.5 to 10 μm. When combined with the finer sensitivity offered by traditional visible interferometry and the coarser sensitivity of conventional shadow moiré, this provides the experimenter the luxury of choosing the sensitivity that is best suited for the required task.

BIBLIOGRAPHY

[1] Verma, K., "Development of Far Infrared Fizeau Interferometry for Real-Time Warpage Measurement of Rough Surfaces," *Ph.D. Dissertation,* Clemson University (2000).

[2] Post, D., Han, B., and Ifju, P., *High Sensitivity Moiré: Experimental Analysis for Mechanics and Materials,* Springer-Verlag (New York, 1994).

[3] Poon, C. Y., Kujawinska, M., and Ruiz, C., "Automated Fringe Pattern Analysis for Moiré Interferometry," *Experimental Mechanics,* Vol. 33, No. 3 (1993), pp. 234-241.

[4] Han, C., "Shadow Moiré Using Non-Zero Talbot Distance and Application of Diffraction Theory to Moiré Interferometry," *Ph.D. Dissertation*¸ University of Maryland – College Park (2005).

[5] Wang, Y., and Hassell, P., "Measurement of Thermally Induced Warpage of BGA Packages/Substrates Using Phase-Stepping Shadow Moiré," *Proc 1997 1st Electronic Packaging Technology Conf,* IEEE/CPMT, Singapore, Oct. 1997, pp. 283-289.

[6] Beckmann, P., and Spizzichino, A., *The Scattering of Electromagnetic Waves from Rough Surfaces*, Macmillan (New York, 1963).

[7] Sinha, J. K., and Tippur, H. V., "Infrared Interferometry for Rough Surface Measurements: Application to Failure Characterization and Flaw Detection," *Optical Engineering*, Vol. 36, No. 8 (1997), pp. 2233-2239.

[8] Munnerlyn, C. R., and Latta, M., "Rough Surface Interferometry Using CO_2 Laser Source," *Applied Optics*, Vol. 7, No. 9 (1968), pp. 1858-1859.

[9] Verma, K., and Han, B., "Far-infrared Fizeau Interferometry," *Applied Optics*, Vol. 40, No. 28 (2001), pp. 4981-4987.

[10] Verma, K., and Han, B., "Real-time Observation of Thermally Induced Warpage of Flip-chip Package Using Far-infrared Fizeau Interferometry," *Experimental Mechanics,* Vol. 44, No. 6 (2004), pp. 628-633.

[11] Kwon, O., Wyant, J. C., and Hayslett, C. R., "Rough Surface Interferometry at 10.6 μm," *Applied Optics*, Vol. 19, No. 11 (1980), pp. 1862-1869.

[12] Hecht, E., *Optics*, Third Edition, Addison-Wesley (Reading, MA, 1998).

[13] *II-VI Infrared: Materials (ZnSe, ZnS, ZnS MultiSpectral, Ge, GaAs, CdTe)*, II-VI, Inc. (2005), http://www.iiviinfrared.com/materials.html.

[14] Talbot, H. F., "Facts Relating to Optical Science, No. IV," *The London and Edinburgh Philosophical Magazine and Journal of Science*¸ Series 3, Vol. 9 (1836), pp. 401-407.

[15] Testorf, M., Jahns, J., Khilo, N. A., and Goncharenko, A. M., "Talbot Effect for Oblique Angle of Light Propagation," *Optics Communications*, Vol. 129 (1996), pp. 167-172.

[16] Ackerman, C. W., "Development of a Real-Time High Sensitivity Shadow Moiré System and its Application to Microelectronics Packaging," *M.S. Dissertation*, Clemson University (2000).

[17] Han, C., and Han, B., "Error Analysis of the Phase-Shifting Technique when Applied to Shadow Moiré," *Applied Optics*, Vol. 45, No. 6 (2006), pp. 1124-1133.

[18] Liao, J. E. A., and Voloshin, A. S., "Enhancement of the Shadow-moiré Method through Digital Image Processing," *Experimental Mechanics*, Vol. 33 (1993), pp. 59-63.

[19] Chen, K. S., Chen, T. Y. F., Chuang, C. C., and Lin, I. K., "Full-Field Wafer Level Thin Film Stress Measurement by Phase-Stepping Shadow Moiré," *IEEE Transactions on Components and Packaging Technologies*, Vol. 27, No. 3 (2004), pp. 594-601.

[20] Zwemer, D., Bajaj, M., Peak, R., Thurman, T., Brady, K., McCarron, S., Spradling, A., Dickerson, M., Klein, L., Liutkus, G., and Messina, J., "PWB Warpage Analysis and Verification using an AP210 Standards-based Engineering Framework and Shadow Moiré," *Proc 5th International Conf on Thermal and Mechanical Simulation and Experiments in Micro-electronics and Micro-Systems*, IEEE, Brussels, Belgium, May 2004, pp. 121-131.

[21] Wei, S., Wu, S., Kao, I., and Chiang, F. P., "Measurement of Wafer Surface Using Shadow Moiré Technique with Talbot Effect," *Journal of Electronic Packaging,* Vol. 120 (1998), pp. 166-170.

[22] Han C., and Han, B., "High Sensitivity Shadow Moiré Using Nonzero-Order Talbot Distance," *Experimental Mechanics*, Vol. 46 (2006), pp. 543-554.

[23] Kafri, O., and Keren, E., "Fringe Observation and Depth of Field in Moiré Analysis," *Applied Optics*, Vol. 20, No. 17 (1981), pp. 2885-2886.

[24] Janssens, J. L., Decraemer, W. F., and Vanhuyse, V. J., "Visibility Depth of Shadow-moiré Fringes in Function of Extend of Light Source and Aperture of Recording System," *Optik*, Vol. 71, No. 2 (1985), pp. 45-51.